Control of interfacial instabilities through variable injection rate in a radial Hele-Shaw cell: A nonlinear approach for late-time analysis

Sajjad Gholinezhad,[1,*] Apostolos Kantzas [1,2] and Steven L. Bryant[1,3]

[1]*Department of Chemical and Petroleum Engineering, University of Calgary, 2500 University Drive NW, Calgary, Alberta, Canada, T2N 1N4*
[2]*PERM Inc. TIPM Laboratory, 3-2221 41 Avenue NE, Calgary, Alberta, Canada, T2E 6P2*
[3]*Canada Excellence Research Chair in Materials Engineering for Unconventional Oil Reservoirs, 750 Campus Drive NW, Calgary, Alberta, Canada, T2N 1N4*

In this paper, the nonlinear behavior of immiscible viscous fingering in a circular Hele-Shaw cell under the action of different time-dependent injection flow rate schemes is assessed numerically. Unlike previous studies which addressed the infinite viscosity ratio (inviscid-viscous flow), the problem is tackled by paying special attention to flows with finite viscosity ratio (viscous flow) in which the viscosity of the displacing and the displaced fluids can have any arbitrary value. Systematic numerical simulations based on a complex-variable formulation of Cauchy-Green barycentric coordinates are performed at different mobility ratios and capillary numbers with a focus on the late-time fully nonlinear regime. Additionally, numerical optimization is used to obtain the optimal flow rate schedule through a second-order weakly nonlinear stability analysis in contrast to previous studies in which the optimal flow rate was obtained entirely based on linear stability analysis. It is demonstrated that, irrespective of the values of the mobility ratio and/or the capillary number, for patterns whose constant injection counterpart exhibits linear flow regime, the curvature-driven relaxation time is comparable with the operational time of the time-dependent injection flow rate controlling schemes, and most of the controlling schemes work very well and suppress the fingering phenomenon remarkably with the maximum recovery improvement of 15%. As the nonlinearity of the system increases, the schemes may still perform well, but their effectiveness is more pronounced in patterns with less nonlinearity in their constant injection counterpart than those with higher nonlinearity. As the nonlinearity increases, the curvature-driven relaxation time becomes longer than the operational time of the schemes, leading to a reduction in their effectiveness. Additionally, it is shown that employment of the second-order weakly nonlinear stability analysis to formulate the objective function does not result in any remarkable variation in the obtained optimal flow rate schedule.

I. INTRODUCTION

Viscous fingering or the Saffman-Taylor instability [1] is perhaps one of the most common interfacial instabilities in fluid dynamics. When a low-viscosity fluid displaces another fluid with higher viscosity in a porous medium or in a narrow space between two parallel plates known as Hele-Shaw cell, the interface between the two fluids starts to deform, and complex fingering patterns develop. Although amplification of these fingering patterns can be beneficial in some applications such as fluid mixing [2], in many practical applications such as enhanced oil recovery (EOR) [3,4] and CO_2 sequestration (CS) [5], such instabilities are quite counterproductive. Therefore, the ability to prescribe strategies which control and eventually suppress the development of these interfacial instabilities is of great importance. In this context, due to the nonlinear behavior of the process, particularly at later times, prediction and controlling of viscous-driven interfacial disturbances in a Hele-Shaw cell has been a challenging topic for a long time and, specifically in recent years, has attracted considerable attention.

The existing literature proposes different strategies to control and possibly suppress the development of viscous fingering instabilities in a Hele-Shaw cell. These strategies can be classified as (1) altering the Hele-Shaw cell conventional geometry [6–13], (2) manipulating the fluid properties [14–18], (3) using time-dependent injection flow rates [19–26], (4) applying an external electric field [27,28], and (5) combining two or more of these strategies [29–33].

A first set of controlling strategies involves modification of the cell geometry. Replacement of the conventional rigid top plate of the cell by an elastic membrane [6–8], changing the gap size over time [9], introduction of a small negative gradient in the gap size in the direction of fluid displacement [10,11], and rotation of both top and bottom plates around the cell vertical symmetry axis [12,13] are some of the geometrical suppression techniques which were shown to be effective in controlling interfacial instabilities.

In the second set of strategies, the properties of the fluids, particularly their viscosity, are altered. Several studies have shown that using non-Newtonian fluids as the displaced and/or displacing fluids can offer opportunities for controlling of the developed pattern [14–16]. Particularly, non-Newtonian fluids with time-dependent rheology have shown promising results [17,18]. Although higher values of surface tension

*sajjad.gholinezha1@ucalgary.ca

can suppress viscous fingers, especially at early flow stages, application of time-dependent surface tension has not been reported in the literature mainly because of the practical difficulties or even impossibility of such a strategy.

A third line of research searches for suppression methods which involve adjusting the injection flow rate in a circular Hele-Shaw cell with radial flow geometry. In contrast to conventional constant injection rate which leads to growth of interfacial instabilities, these methods try to control the instabilities by employing an ideal time-dependent injection flow rate. The oldest strategy of this type is cyclic injection in which the displacing fluid is injected over properly distributed intervals of time [19,20]. Another interesting scheme of this type focuses on maintaining a fixed number of fingers. It has been shown that, by using an injection flow rate which scales with $t^{-1/3}$, the number of emerging fingers can be controlled [21–23]. Although this protocol does not remove the fingers and still some fingers exist at the interface, it tunes the interface into an n-fold symmetric structure with a preassigned number of emerging fingers which does not multiply over the course of time. Using a simple piecewise constant two-step injection flow rate, in which a proper higher injection rate follows a proper lower injection rate, is another control technique which can minimize the development of interfacial instabilities. It has been demonstrated that, for a finite volume of injected fluid in a given time, applying this protocol can lead to a one-order-of-magnitude reduction in the size of the fingers compared with the conventional constant injection flow rate [24]. Another interesting control scheme of this type systematically looks for an optimum injection flow rate which minimizes the final amplitude of the emerging fingers. Based on linear stability analysis in a radial geometry, it has been demonstrated that, in the limit of high capillary numbers, such an optimal injection flow rate is a linear function of time with a positive slope [25]. This scheme was later extended for arbitrary values of capillary numbers, leading to an optimal flow rate which is a closed-form analytical function of time [26].

An alternative line of research concentrates on trying to suppress the interfacial instabilities by applying an external electric field along the surface of the cell. It has been shown that positive electric current generates an electro-osmotic force which restrains the establishment of interfacial disturbances by reducing the apparent viscosity of the resident fluid [27,28].

Finally, in the last set of strategies, a combination of two different strategies has been investigated. Combination of optimal flow rate with rotating cell [29], combination of optimal flow rate with time-dependent viscosities [30,31], and combination of tapered cell with time-dependent viscosities [32,33] are some of the strategies which have recently been shown to be effective on reducing viscous fingering.

Despite the usefulness of the existing controlling strategies to suppress interfacial instabilities in many applications, except the time-dependent flow rate strategy, the application of the other schemes in EOR and CS is associated with numerous limitations and challenges. The major practical challenge is that modification of the geometry of underground oil reservoirs and aquifers, particularly in a time-dependent manner, is impossible. This limitation hinders the practical application of

geometrical controlling strategies in EOR and CS. Although thermal methods have been successfully applied to decrease the viscosity of resident oil in oil reservoirs, such a change is usually expensive and limited to specific conditions [34]. Additionally, owing to the inherent low viscosity of resident brine in aquifers, considerable modification of its viscosity is impossible. Regarding the viscosity of the injecting fluid, usually polymers are added to the injecting fluid (usually water or brine) to increase its viscosity. However, limitations such as the high cost of polymers, pore plugging, and polymer degradation at harsh conditions of temperature and salinity hinder their widespread applications [30,35]. Due to these limitations, the application of the strategies which alter the fluid viscosity is not always feasible. Regarding the application of an electric field, both resident and injection fluids are required to be highly conductive. Additionally, because of the requirement of high voltage, the high cost of generating a large-scale electric field is another limitation of this method. As a result, it becomes practically impossible to use electric fields for a real application of instability control in EOR and/or CS.

Following the above discussion, manipulation of the rate at which the displacing fluid is injected seems to be the most convenient and practical way of controlling the interfacial instabilities in real porous media applications. Although the effectiveness of some of these simple controlling schemes has been confirmed by linear stability analysis [24–26], sophisticated numerical simulations (for inviscid-viscous flow) [29], and meticulous experiments [25], their late-time performance particularly for viscous-viscous displacement have not been investigated systematically. Specifically, the late-time performance of the scheme proposed by Batista *et al.* [26] for arbitrary capillary numbers has not been investigated in detail.

In this paper, to access the response of the displacement at later time stages of the evolution, we explore numerically the dynamics and control of interfacial instabilities under the action of different time-dependent flow rate schemes in a circular Hele-Shaw cell in which a fluid with nonzero viscosity displaces another immiscible fluid. Unlike previous studies which addressed the infinite viscosity ratio (i.e., inviscid-viscous flow), we tackle the problem by paying special attention to flows with finite viscosity ratio (i.e., viscous flow) in which the viscosity of the displacing and displaced fluids can have any arbitrary values. Systematic numerical simulations based on complex-variable formulation of Cauchy-Green barycentric coordinates [36] are performed at different viscosity ratios and capillary numbers with a focus on late-time fully nonlinear regime. Additionally, we go one step further by, in the spirit of Dias *et al.* [25] and Batista *et al.* [26], deriving an optimal injection flow rate through second-order weakly nonlinear stability analysis in contrast to the previous studies in which an optimal flow rate was obtained entirely based on linear stability analysis.

It should be noted that, in this paper, investigation of the optimal flow rate schedule is undertaken assuming that the time scale for changing the injection flow rate is small compared with the time scale required for curvature-driven relaxation of fingers. As will be shown later, the time scale required for curvature-driven relaxation is notoriously long compared with the typical fingering time scales, and thus,
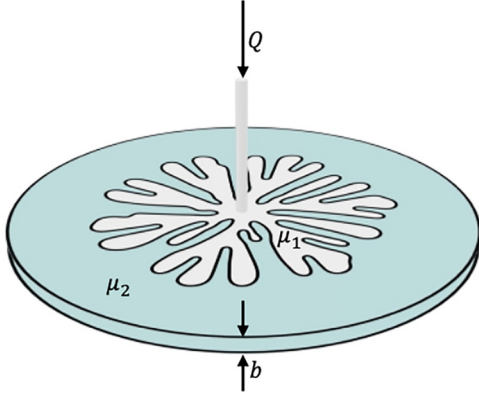
FIG. 1. Schematic representation of the standard radial Hele-Shaw cell.

practically, it is not feasible to wait for such long time scales.

The reminder of this paper is organized as follows. In Sec. II A, the governing equations of fluid flow in a circular Hele-Shaw cell are presented. In addition to summarizing our state of knowledge about the existing time-dependent flow rate schemes, an injection flow rate policy is provided in Sec. II B. The details of the employed numerical framework which enable us to gain access to the nonlinear dynamics of the system are described in Sec. II C, while Sec. III reports the results and the relevant discussions, particularly on the effect of governing parameters of the system (i.e., mobility ratio and capillary number) in the presence of nonlinear effects. Finally, the paper ends with Sec. IV, where our final remarks are briefly summarized, and some perspectives are outlined.

II. MATHEMATICAL MODEL

A. Governing equations

Consider a circular Hele-Shaw cell which is composed of two flat stationary parallel plates of infinite radius separated by a gap of constant thickness b (Fig. 1). Through a tiny orifice located at the center of the cell, fluid 1 with the constant arbitrary viscosity of μ_1 is injected radially at a volumetric flow rate of Q which may vary with time. Fluid 2 with the constant arbitrary viscosity of μ_2 initially occupies the cell except a small part with the average radius of R_0 around the orifice and is removed from the outer boundary of the cell with a constant atmospheric pressure. It is assumed that the fluids are incompressible and immiscible with an interfacial tension of arbitrary value σ. Additionally, it is assumed that the cell is horizontal and b is much smaller than the cell radial extent ($b/R \ll 1$), and thus, the system can be considered a quasi-two-dimensional system by neglecting inertial effects (i.e., both Bond and Reynolds numbers are very small). The simply connected planar domains occupied by fluids 1 and 2 are denoted by Ω_1 and Ω_2, respectively, while $\partial\Omega$ shows the interface between the two fluids. Under these conditions, the fluid flow can be described by the following equations:

$$\nabla \vec{v}_k = 0, \quad k = 1, 2, \tag{1}$$

$$\vec{v}_k = -M_k \nabla P_k, \quad k = 1, 2, \tag{2}$$

where $\vec{v}_k$ and P_k show the vertically averaged velocity and pressure of fluid k, respectively. The first equation is the continuity equation, while the second equation is Darcy's law. Here, M_k is the mobility of fluid k which is related to b and μ by

$$M_k = \frac{b^2}{12\mu_k}, \quad k = 1, 2. \tag{3}$$

At the interface which is initially located at R_0, we have the following boundary conditions:

$$P_1 - P_2 = \sigma\left(\kappa + \frac{2\cos\theta}{b}\right), \tag{4}$$

$$\vec{v}_1\hat{n} = \vec{v}_2\hat{n}, \tag{5}$$

where κ is the signed curvature of the interface, and $\hat{n}$ represents the unit outward normal vector. Here, θ shows the contact angle. The first equation is the dynamic boundary condition which describes the pressure jump due to the interfacial tension through the Young-Laplace equation, while the second equation is the kinematic boundary condition which imposes the continuity of the normal velocities at the interface. In this paper, the gap thickness across the cell is constant, and thus, the gradient of the curvature in the direction perpendicular to the cell bounding plates is zero. This way, the perpendicular curvature does not affect the interface motion, and the only contribution of capillary pressure is the lateral curvature (i.e., the curvature in the bounding plates of the cell). Accordingly, Eq. (4) can be simplified to

$$P_c^{\text{eff}} = P_1 - P_2 - \frac{2\cos\theta}{b} = \sigma\kappa. \tag{6}$$

It should be noted that the effects of thin wetting film left behind and viscous normal stresses at the interface are also neglected.

B. Weakly nonlinear stability analysis and optimal flow rate

In this section, to understand the stability of interface, the weakly nonlinear stability analysis is reviewed. For simplicity, we consider polar coordinates at the plane of the flow and assume that the initially circular interface is slightly distorted. The perturbed interface $\mathcal{R}$ can be described as [37]

$$\mathcal{R}(\phi, t) = R(t) + \zeta(\phi, t), \ 0 \leqslant \phi \leqslant 2\pi, \quad |\zeta| \ll R, \tag{7}$$

where $R(t)$ is the radius of the equivalent unperturbed interface at time t and can be obtained by

$$R(t) = \sqrt{R_0^2 + \frac{1}{\pi}\int_0^t Q(t')dt'}, \tag{8}$$

and ζ is the arbitrary perturbation which can be represented as the following complex Fourier series:

$$\zeta(\phi, t) = \sum_{n=-\infty}^{+\infty} \zeta_n(t)\exp(in\phi), \tag{9}$$

where i is the imaginary unit, n is the integer azimuthal wave number, and ζ_n is the perturbation amplitude of mode n. Here, our main task is to obtain the weakly nonlinear time evolution of ζ accurate to second order. This is a lengthy derivation

which was presented by Miranda *et al.* [37]. To avoid cluttering this paper with too much detail, only the final equation is presented here which can be written as follows:

$$\dot{\zeta}_n = \lambda_n \zeta_n + W_n(t), \tag{10}$$

where the overdot shows the total time derivative and

$$\lambda_n = \frac{Q}{2\pi R^2}(A|n| - 1) - \frac{\gamma}{R^3}|n|(n^2 - 1), \tag{11}$$

$$W_n(t) = \sum_{p \neq 0}(F_{n,p} + \lambda_p G_{n,p})\zeta_p \zeta_{n-p}, \tag{12}$$

$$F_{n,p} = \frac{|n|}{R}\left\{\frac{QA}{2\pi R^2}\left[\frac{1}{2} - \text{sgn}(np)\right] - \frac{\gamma}{R^3}\left[1 - \frac{p}{2}(3p + n)\right]\right\}, \tag{13}$$

$$G_{n,p} = \frac{1}{R}\{A|n|[1 - \text{sgn}(np)] - 1\}, \tag{14}$$

$$A = \frac{MR - 1}{MR + 1}, \tag{15}$$

$$\gamma = \frac{b^2 \sigma}{12(\mu_1 + \mu_2)}, \tag{16}$$

where MR is the mobility ratio of the fluids and can be expressed by

$$MR = \frac{M_2}{M_1}. \tag{17}$$

Equation (10) is called the second-order mode coupling equation of the Saffman-Taylor instability which describes the temporal evolution of the interfacial instabilities in a circular Hele-Shaw cell. The first term on the right-hand side is the purely linear growth of the perturbation, while the second term denotes the weakly nonlinear contribution. This equation is a nonhomogeneous linear ordinary differential equation which can be easily solved using integrating factor [37]:

$$\zeta_n(t) = \zeta_n(0)\exp\left(\int_0^t \lambda_n dt'\right)$$
$$\times \left[1 + \int_0^t \frac{W_n(t')}{\zeta_n(0)\exp\left(\int_0^{t'} \lambda_n dt''\right)}dt'\right]. \tag{18}$$

At the linear level, the number of emerging fingers is given by the mode with the maximum growth rate which can be calculated by $\partial \lambda_n / \partial n|_{n=n_{\max}} = 0$, leading to [37]

$$n_{\max} = \sqrt{\frac{1}{3}\left(1 + \frac{A\dot{R}R^2}{\gamma}\right)}, \tag{19}$$

where

$$\dot{R} = \frac{Q}{2\pi R}. \tag{20}$$

In time-dependent injection flow rate controlling schemes of interfacial instability, the goal is to search for a proper injection flow rate which minimizes or even suppresses the growth of fingers, i.e., $\zeta_n(t_f)$, in which t_f is the final time of the process. Due to the plethora of possibilities for time functionality of the injection flow rate, several scenarios have been proposed in the existing studies. The simplest scenario is cyclic injection which involves distributing the injection process over proper time intervals rather

than monotonic constant injection rate [19]. Each cycle starts with an injection stage in which a finite volume of fluid is injected for a finite period. In the second stage, the injection process is stopped, and the orifice is shut in for a finite period, which may be different from the injection period. During the shut-in period, the driving force for the finger development is eliminated, and consequently, the interfacial tension which acts as the stabilizing force retracts the developed fingers [20]. In practice, the whole process can consist of several cycles, depending on the technical and economical limitations. In this paper, for the sake of consistency, the total amount of the injected fluid and the final time are kept constant for all the tested methods. We consider four cycles as the typical number of cycles with equal time intervals for injection and shut-in stages.

The second time-dependent flow rate controlling scheme focuses on prescribing the number of fingers. From Eqs. (19) and (8), by integrating $\dot{R}$ over time and keeping $n_{\max}$ constant, it can be shown that, if Q is adjusted to follow the following equation, the interface will evolve by maintaining $n_{\max}$ symmetrical fingers which grow but do not multiply as time evolves [22,23]:

$$Q = \frac{2\pi}{\sqrt[3]{3}}\left[\frac{\gamma}{A}\left(3n_{\max}^2 - 1\right)\right]^{2/3} t^{-1/3}. \tag{21}$$

This strategy was proposed by Bataille [21] using linear stability analysis and was later further confirmed by weakly nonlinear, numerical, and experimental studies [22,23,38]. Although this technique offers a valid procedure to prescribe the number of nonsplitting fingers which might improve the performance of some physical systems, it does not quite remove the fingers, and the evolving fingers have considerable sizes. Therefore, we do not investigate this technique further, as the focus of this paper is only on efficient time-dependent flow rates which seek ultimate suppression of the fingers and are more desired for EOR and CS applications. For a detailed description of this method, the interested reader is referred to Refs. [22,23,38].

Based on linear stability analysis, it has been shown that employment of a simple piecewise constant two-step injection flow rate can restrain interfacial instabilities in a radial Hele-Shaw cell at a specific scenario. Since in a radial Hele-Shaw cell velocity decreases with the radial distance, setting of a lower injection rate for the first stage and a higher injection rate for the second stage is the only two-stage scenario which can outperform the conventional constant injection flow rate for a finite volume of injected fluid in a given time. The duration of each stage and the corresponding flow rates are a function of the system properties which can be obtained by minimizing the amplitude of the fingers at the end of the process by recalling the constraint that, for the final time, the amplitude of the fingers with maximum growth rate which were created and developed at the second stage must be the same as the amplitude of the fingers with maximum growth rate which were created at the first stage and developed during both first and second stages [24]. Indeed, such a minimization procedure does not lead to a closed-form analytical expression, and therefore, numerical optimization techniques are required to find the optimal duration and the flow rates of

the stages. In this paper, a numerical optimization framework based on sequential least squares programming (SLSQP) was employed to solve the problem. For a detailed discussion of the method, the reader is referred to Dias *et al.* [24].

In an interesting control scheme of this type, by systematically searching for the best injection flow rate which minimizes the linear perturbation amplitude, through the Euler-Lagrange equation, it has been demonstrated that, in the limit of high capillary numbers, such an ideal injection flow rate scales linearly with time as [25]

$$Q(t) = 2\pi \frac{R_f - R_0}{t_f} \left(R_0 + \frac{R_f - R_0}{t_f} t \right), \quad (22)$$

where R_f is the interface equivalent average radius at t_f. Considering the necessity of a higher injection following a lower injection for the two-stage strategy, this scheme is expectable. The effectiveness of this method was verified by analytical, numerical, and experimental studies [25,29]. A detailed derivation of this scheme can be found in Ref. [25]. This scheme, hereafter referred to as *linear approximate*, was later generalized for arbitrary values of capillary numbers, and by minimizing the linear perturbation amplitude through the Hamiltonian equation, it was shown that the optimal flow rate can be written as [26]

$$Q(t) = \left(\frac{c_1}{9A^2} \right) \frac{2\pi \left[(c_1 t + c_2)^2 - \frac{3\gamma(A+1)}{2} \right]}{\left[(c_1 t + c_2)^3 - \frac{9\gamma(A+1)}{2}(c_1 t + c_2) \right]^{1/3}}, \quad (23)$$

where c_1 and c_2 are constants which can be determined by the boundary conditions: $R(0) = R_0$ and $R(t_f) = R_f$. This scheme is referred to as *linear exact* hereafter. A detail derivation of this scheme can be found in Ref. [26].

While the last two optimal flow rates offer an efficient way to suppress interfacial instabilities, they do not provide the true minimum of the whole nonlinear perturbation amplitude. The effect of nonlinear terms becomes important at later times when the mechanisms other than spreading are activated. However, according to Eq. (12), for a given mode, the whole nonlinear amplitude depends on the amplitude of other modes which makes it very difficult (and most probably impossible) to minimize it analytically. In this paper, we seek to obtain the true optimal point of the problem using nonlinear optimization. In this sense, Eq. (18) is minimized using the SLSQP optimization algorithm of the SciPy library in Python. To have a consistent comparison with previous schemes, for a given total time, the total volume of injected fluid was kept constant and fed in as the constraints to the employed optimization algorithm. The problem is then formulated as

$$\zeta_{n_{\max}}(t_f) = \zeta_{n_{\max}}(0) \exp\left(\int_0^{t_f} \lambda_{n_{\max}} dt' \right)$$
$$\times \left[1 + \int_0^{t_f} \frac{W_{n_{\max}}(t')}{\zeta_{n_{\max}}(0) \exp\left(\int_0^{t'} \lambda_{n_{\max}} dt'' \right)} dt' \right], \quad (24)$$

constrained to

$$\int_0^{t_f} Q \, dt = Q_{\text{Ref}} t_f, \quad (25)$$

where Q_{Ref} is the injection flow rate of the reference constant injection rate process.

C. Numerical simulation

While weakly nonlinear and particularly linear stability analysis offers a helpful tool to understand the qualitative dynamic behavior of the problem and derive different controlling strategies, its validity is restricted to a short period of time after the onset of the instability beyond which nonlinear dynamics takes over. It is therefore necessary to perform numerical simulations to explore the full nonlinear dynamics of the problem and visualize the advanced time evolution of the interface. In this section, to investigate the range of validity of the existing as well as the proposed controlling scheme, we conduct a full numerical simulation of the problem. The numerical method employed here is like the complex-variable formulation of Cauchy-Green barycentric coordinates developed in Ref. [36]. In this framework, which is a variant of boundary integral methods, only the fluid-fluid interface is tracked which reduces the computational cost remarkably and allows us to efficiently simulate the process. If we define the following transformation:

$$\phi_k = M_k P_k, \quad k = 1, 2, \quad (26)$$

from Eq. (1), it can be easily shown that ϕ is a potential function which obeys Laplace's equation:

$$\nabla^2 \phi_k = 0, \quad k = 1, 2. \quad (27)$$

Substituting Eq. (26) into Eq. (4) gives the following expression for the dynamic boundary condition:

$$\frac{\phi_1}{M_1} - \frac{\phi_2}{M_2} = \sigma \kappa, \quad (28)$$

while the kinematic boundary condition can be written as

$$\vec{\nabla} \phi_1 \hat{n} = \vec{\nabla} \phi_2 \hat{n}. \quad (29)$$

Now to simplify the solution procedure, we switch from the real domain to the complex domain by denoting the point (x, y) in the real domain by $z = x + iy$. This switching reduces the problem dimension by one. The model equations in the complex domain can be formulated as

$$\nabla^2 \phi_k(z) = 0, \quad k = 1, 2, \quad (30)$$

$$\frac{\phi_1(z)}{M_1} - \frac{\phi_2(z)}{M_2} = \sigma \kappa(z), \quad (31)$$

$$\langle -\vec{\nabla} \phi_1, \hat{n}(z) \rangle = \langle -\vec{\nabla} \phi_2, \hat{n}(z) \rangle. \quad (32)$$

At this point, to further simplify the solution, we reformulate the problem as an evolution problem for the interface. Consider a holomorphic complex potential W whose real part is equal to ϕ [36]:

$$W_k = \phi_k + \psi_k i, \quad k = 1, 2. \quad (33)$$

Using the Cauchy-Riemann theorem and Green's function for the Laplacian in the plane, the governing equations can be rephrased in terms of W [36]:

$$W_k(z) = \frac{Q}{2\pi b} \ln(z) + f_k(z), \quad k = 1, 2, \quad (34)$$

$$\mu_1 \text{Re}[W_1(z)] - \mu_2 \text{Re}[W_2(z)] = \frac{b^2 \sigma}{12} \kappa(z), \quad (35)$$

$$\text{Re}[W_1'(z)\hat{n}(z)] = \text{Re}[W_2'(z)\hat{n}(z)], \quad (36)$$

where f_k is an analytic function on Ω_k. By applying Cauchy's integral formula, the value of f_1 at any point inside Ω_1 can be calculated from its value on the interface $\partial\Omega$:

$$f_1(z) = \frac{1}{2\pi i} \oint_{\partial\Omega} \frac{f_1(\omega)}{\omega - z} d\omega. \tag{37}$$

If we discretize the input interface $\partial\Omega$ into m elements to get the closed polygon $\hat{\Omega}$, by assuming that the value of f_1 on each edge is a linear interpolation between the two end points of that edge and then analytically calculating the edge integrals and rearranging the terms, the integral in Eq. (37) can be discretized as [36]

$$f_1(z) = \sum_{j=1}^{m} C_j(z) f_1(z_j). \tag{38}$$

Here, C is the Cauchy-Green coordinate of the point z which can be found in Ref. [39]. Because f_2 is holomorphic on Ω_2, using Cauchy's integral formula for unbounded domain, we have [36]

$$f_2(z) = \sum_{j=1}^{m} E_j(z) f_2(z_j), \tag{39}$$

where

$$E_j(z) = C_j(a) - C_j(z), \tag{40}$$

where a is an arbitrary point inside Ω_1. Substituting Eqs. (38) and (39) into Eq. (34) and then substituting the resulting equations into Eqs. (35) and (36) and rearranging the terms yields

$$\sum_{j=1}^{m} \{\mu_1 \text{Re}[C_j(z)]\text{Re}[f_1(z_j)] - \mu_1 \text{Im}[C_j(z)]\text{Im}[f_1(z_j)] - \mu_2 \text{Re}[E_j(z)]\text{Re}[f_2(z_j)] + \mu_2 \text{Im}[E_j(z)]\text{Im}[f_2(z_j)]\}$$

$$= (\mu_2 - \mu_1)\frac{Q}{2\pi h} \ln|z| + \frac{b^2 \sigma}{12} \kappa(z), \tag{41}$$

$$\sum_{j=1}^{m} \{\text{Re}[D_j(z)\hat{n}(z)]\text{Re}[f_1(z_j)] - \text{Im}[D_j(z)\hat{n}(z)]\text{Im}[f_1(z_j)] - \text{Re}[F_j(z)\hat{n}(z)]\text{Re}[f_2(z_j)] + \text{Im}[F_j(z)\hat{n}(z)]\text{Im}[f_2(z_j)]\} = 0, \tag{42}$$

where D_j and F_j are the first derivatives of C_j and E_j, respectively. The expressions for these terms can be found in Ref. [39]. At this point, each edge of the polygon $\hat{\Omega}$ is sampled at four points on which Eqs. (41) and (42) are constructed, leading to a linear set of equations which is then solved by SciPy lsq_linear to obtain f_1 and f_2 at m vertices of the polygon $\hat{\Omega}$. The interface normal velocity at $\hat{\Omega}$ vertices is then calculated using the following relation [36]:

$$v_n = -\text{Re}[W_1'(z)\hat{n}(z)], \tag{43}$$

then the vertices of $\hat{\Omega}$ advance using the following equation:

$$\frac{d\hat{\Omega}}{dt} = v_n, \tag{44}$$

which was integrated using a first-order Euler method with an adaptive time step as follows:

$$dt = \frac{\alpha l_{\text{ave}}}{v_{\text{max}}}, \tag{45}$$

where l_{ave} is the average edge length and v_{max} is the maximum velocity observed in the interface. The parameter α controls the interface maximum displacement at each time step and is chosen such that it guarantees convergence without reducing efficiency. At the next step, the new interface position is interpolated and sampled using a cubic spline, and the procedure is repeated until the final time. In this paper, the SciPy built-in interpolation function was employed to interpolate and sample the interface. The sampling process is curvature-based in which the density of the sampling points is higher in the highly curved areas. As the interface grows, the number of sampling points adaptively increases to keep the edge length constant. The initial interface was constructed using the following for-

mula [29]:

$$\hat{\Omega}(\phi, 0) = R_0 \left\{ 1 + \epsilon \sum_{j=2}^{13} \cos[j(\phi - 2\pi\chi_j)] \right\}, \tag{46}$$

where R_0 is the radius of the initial interface, and ϵ is the initial amplitude. Here, χ is a random number between 0 and 1. It is worth noting that, in this paper, the dynamic initiation of noise was neglected, and it was assumed that the noise can be fully described through the perturbations at the initial interface. The main motivation for this assumption originates from the fact that, according to Eq. (18), the growth of perturbations is an exponential function of time, and thus, the perturbations which are created later play a less significant role. Another motivation is that dynamic generation of noise is prone to violation of material balance which is a serious problem.

III. RESULTS AND DISCUSSION

In this section, the results for the existing as well as the proposed time-dependent flow rate controlling strategies are presented and compared with those of the constant injection flow rate with emphasis upon late-time nonlinear dynamics. We begin by validating our numerical framework through comparison of our numerical results with the published experiments conducted under identical conditions. Figure 2 shows the experimental results obtained by Bischofberger *et al.* [40] and their replication by our numerical framework for three different viscosity ratios in descending order. For all cases, the initial interface is of the form of Eq. (46) with $R_0 = 0.004$ m and $\epsilon = 0.001$. The relevant physical properties of the experiments are given in the figure caption. While the visual comparison of the corresponding cases qualitatively verifies
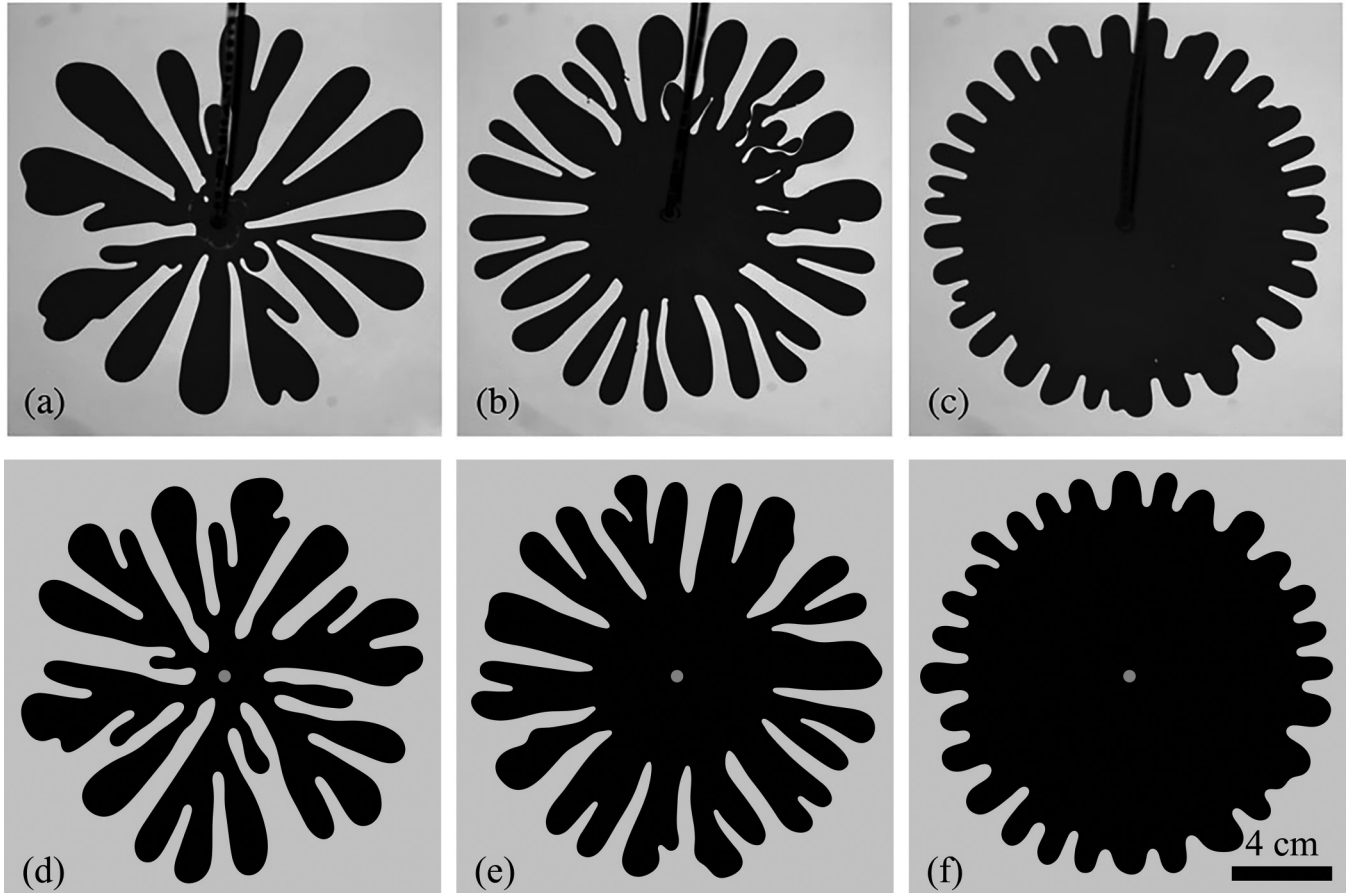
FIG. 2. (a)–(c) Experimental patterns from Bischofberger *et al.* [40], reproduced with permission from Royal Society of Chemistry, and (d)–(f) the corresponding numerical results. (a) and (d) $\mu_1 = 0.99$ mPa s, $\mu_2 = 296.7$ mPa s, MR $= 299.70$. (b) and (e) $\mu_1 = 46.6$ mPa s, $\mu_2 = 345.1$ mPa s, MR $= 7.41$. (c) and (f) $\mu_1 = 224.4$ mPa s, $\mu_2 = 530.3$ mPa s, MR $= 2.36$. In all experiments, black fluid is a dyed glycerol-water solution, while the colorless fluid is a silicone oil which fully wets the cell surface. Additionally, $b = 254\,\mu$m, $Q = 10$ mL/min and $\sigma = 26 \pm 2.5$ mN/m.

the numerical framework, we have also considered three geometrical measures to quantify the similarity. The first metric, which is called the *normalized interfacial length*, measures how far the interface is from a circle and is defined as [41,42]

$$\mathcal{I} = \frac{L}{2\sqrt{\pi A}}, \tag{47}$$

where L is the arc length of the interface, and A is the area of the zone swept by the displacing fluid. Basically, $2\sqrt{\pi A}$ is the perimeter of a circle whose area is A, and consequently, a circular area has the minimum value of $\mathcal{I}$ which is 1. For any other shape, $\mathcal{I} > 1$. The second metric, which is referred to as the *modified roughness ratio*, is a measure of the average length of the fingers rescaled by a characteristic length and is defined as

$$\mathcal{C} = \frac{R_O - R_I}{R_I}, \tag{48}$$

where R_O is the average distance of the tips of the fingers from the injection point, and R_I is the average distance of the valleys of the fingers from the injection point. For a fully stable flow with no fingering, $\mathcal{C} = 0$, and it increases as the fingers grow. The SciPy Signal library was employed to identify the local tips and valleys. The third metric, which is called *areal sweep*

efficiency, is a common measure in petroleum engineering which measures the effectiveness of the injection process in terms of the swept area. It is defined as

$$E_A = \frac{A}{A_c} \times 100, \tag{49}$$

where A_c is the area of the smallest circle with the center at the injection point that circumscribes the entire swept area. The calculated values of $\mathcal{I}$, $\mathcal{C}$, and E_A for the patterns in Fig. 2 are given in Table I. We observe that, in correspondence with $\mathcal{I}$, $\mathcal{C}$, and E_A, the numerical results agree very closely with the experimental data with the maximum error of 24, 27, and 5%, respectively. It is worth noting that, in our numerical simulation, the effects of thin wetting film left behind the displaced fluid and the viscous normal stress were neglected [43–45]. Additionally, the real experiment is a three-dimensional phenomenon which has been simulated as a quasi-two-dimensional process in our simulations [46]. Another important fact is that, in viscous fingering, the initiation of fingers is inherently a stochastic process in which their amplitude, wavelength, phase, spatial distribution, and temporal distribution are unknown, making the real initiation of fingers inaccessible to numerical simulations [47]. As mentioned before, in this paper, the dynamic initiation of noise was

TABLE I. Comparison of the experimental and simulation results in terms of the geometric measures.

Patterns	Mobility ratio	$\mathcal{I}$		$\mathcal{C}$		$E_A(\%)$	
		Experimental	Numerical	Experimental	Numerical	Experimental	Numerical
a, d	299.70	5.62	5.53	1.46	1.06	50.2	51.2
b, e	7.41	5.68	4.34	0.79	0.68	63.0	66.4
c, f	2.36	2.76	2.12	0.21	0.19	83.0	81.3

neglected, and it was assumed that the noise can be fully described through the perturbations at the initial interface. These effects can be responsible for the observed discrepancies between the experimental data and our numerical simulation results. Another important observation is that, at the top-right quarter of the pattern in Fig. 2(b), some fingers were developed in the perpendicular direction, and their azimuthal development is comparable with their radial propagation. The reason is that, for the conditions of Fig. 2(b), according to Lenormand's criteria [48,49], the invasion is under the transition regime between viscous fingering and capillary fingering in which, because of the competition between the viscous and capillary forces, fingers develop at both radial and azimuthal directions. Although the simulated pattern in Fig. 2(e) does not show the competition to the same extent as the experimental pattern, the thick bases of the fingers are a symptom of later competition. Despite these discrepancies, our simulation results are the closest simulations to the experimental data without any limitation on fluid viscosities.

It is worth noting that we have also examined the effect of the number of sampling points on the results by employing a decreasing edge length. The simulations indicate that, below a threshold edge length, the developed patterns agree both qualitatively and quantitatively (see Appendix A). Additionally, we have tested the effect of the distribution of sampling points by examining both curvature-based and uniform (equally spaced) arc-length-based sampling approaches [50]. The results showed that, to have the same pattern, the uniform arc-length-based sampling requires smaller edge length which leads to a higher number of sampling points and consequently higher computational cost, but below a threshold edge length, its results exactly coincide with the curvature-based sampling approach. It is also worth noting that, for a perfect circular interface with no perturbation at the initial interface, with injecting the fluid, the circle grows proportionally, and only at very late time, due to the numerical errors, some fingers emerge. Examination showed that the initial number of fingers and their phase only impact the qualitative behavior of the pattern by changing the phase of the developed fingers, but they do not change the quantitative measures remarkably. Testing the initial amplitude of the fingers showed that it has a profound effect on the developed pattern, both qualitatively and quantitatively. Comparison of the emerging patterns for initial amplitudes of 0.0001, 0.0005, 0.001, 0.002, and 0.005 showed that, with increasing the initial amplitude, longer fingers developed in the system, which is consistent with the predictions of Eq. (18) in which the temporal growth of the fingers is directly proportional to their initial amplitude. The employed value of $\epsilon = 0.001$ has been chosen such that it provides a closer match to the experiments. However, it

should be noted that the results are insensitive to small variations in the employed initial amplitude. Finally, comparison of the volume of the developed patterns with the volume of the injected fluid shows deviations <5%, meaning that the numerical framework is mass conservative.

We now take the advantage of the developed numerical framework to systematically examine the effect of the governing parameters on the performance of the existing and the proposed time-dependent flow rate controlling schemes when a prescribed volume of the displacing fluid is injected over a prescribed period. Following the existing literature, all the governing parameters are combined into two dimensionless numbers: mobility ratio (MR), which was already defined in Eq. (17), and capillary number at R_f which is defined as

$$\mathrm{Ca} = \frac{Q_{\mathrm{Ref}}(\mu_2 - \mu_1)}{2\pi R_f b\sigma}. \tag{50}$$

To test the effect of MR, we vary its value by three orders of magnitude by taking the values of 2, 10, 100, and 1000 while maintaining a constant $\mathrm{Ca} = 5 \times 10^{-3}$ (referred to as set MR). Similarly, to test the effect of Ca, its value is varied by three orders of magnitude by taking 1.5×10^{-3}, 1.5×10^{-2}, 1.5×10^{-1}, and 1.5 while keeping a constant $\mathrm{MR} = 100$ (referred to as set Ca). For all cases, only the viscosity values are changed, and the other system parameters are kept constant. Here, $b = 254\,\mu\mathrm{m}$, $Q_{\mathrm{Ref}} = 10$ mL/min, and $\sigma = 24.57$ mN/m were set for all cases. To test the effect of MR, $R_f = 0.0850$ m was set, while to test the effect of Ca, $R_f = 0.02833$ m was set. The value of the physical parameters was set based on common radial Hele-Shaw cell experiments. The employed flow rate policies in the first set of simulations (set MR) were calculated and plotted in Fig. 3. By examining different policies for different values of MR, it is quite evident that, for all tested values of MR, the ideal flow rate policy obtained by Dias *et al.* [25], Batista *et al.* [26], and this paper coincide. The calculated value of $A\dot{R}R^2/\gamma$ for the range of $[R_0 = 0.004, R_f = 0.085]$ is in the range of $[316, 6720]$ which is always $\gg 1$, indicating that, for the range of tested parameters in this section, the approximation employed by Dias *et al.* [25] is valid, leading to the same flow rate functionality for the approximate policy of Dias *et al.* [25] and the exact policy of Batista *et al.* [26]. Additionally, it seems that the contribution of the nonlinear terms in Eq. (18) is negligible compared with the linear term, and thus, inclusion of the nonlinear terms did not result in any remarkable difference in the obtained policy compared with Dias *et al.* [25] and Batista *et al.* [26].

Figure 4 shows the time evolution of the interfacial patterns for different mobility ratios under the action of different flow rate schemes. The patterns are plotted at equal time
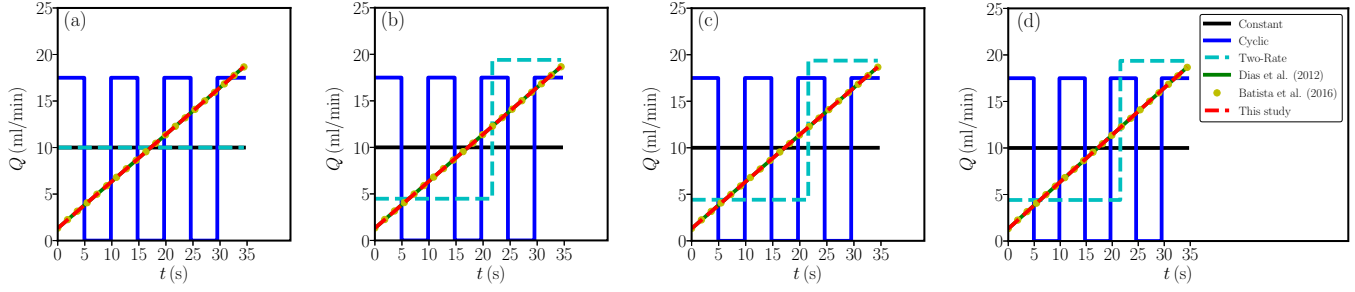
FIG. 3. Employed injection flow rate policies for different values of MR, (a) MR = 2, (b) MR = 10, (c) MR = 100, and (d) MR = 1000.

intervals of $t_f/10$, where t_f is the process final time. Because of the same functionality of linear-approximate and linear-exact schemes, in Fig. 4, only one row was considered for both, and the resulting scheme was simply referred to as *linear*. By scrutinizing the top row of Fig. 4, we observe that, for the conventional constant injection rate, regardless of the value of MR, all patterns evolve to fingered structures, although the length and number of the fingers and overall shape of the patterns are different for different values of MR. While MR = 2 shows only the finger-spreading mechanism, the other three higher values of MR show secondary instability mechanisms of shielding (i.e., competition), tip splitting, and side branching to some extent in addition to spreading. Initially, the interface is almost circular with no visible fingers. As the time evolves, the interface undulates, and the fingers start to emerge. As the injection continues, the fingers spread, and their tips get blunt, forming a fanlike structure. Spreading continues until the finger width reaches a critical value, above which the tip of the finger splits to form second-generation fingers. Fingers of different sizes compete, and smaller fingers are shielded by the larger neighbor fingers. Sometimes, smaller fingers evolve from the lateral sides of more established larger fingers. An interesting observation is that, for higher values of MR, as time progresses, points located on fjords do not move away from their starting locations effectively, creating the commonly named stagnation points, while for lower values of MR, such stagnation points are not encountered, and the fjords keep moving away from their creation point as time advances. This is one of the main dynamic aspects of viscous fingering which was not captured in single-phase flow simulation of the process (with infinite MR), while the employed two-phase flow simulation in this paper (with finite MR) has successfully captured it. These findings are in line with previous two-phase flow simulations presented in Refs. [51,52].

Qualitatively, it is apparent that the cyclic injection policy intensified the fingering phenomenon for all tested cases, particularly for higher values of MR. Although it did not affect the initial number of developed fingers, the area which was fully swept is less than that of the constant injection rate. The physical explanation for the failure of the cyclic

protocol rests on the fact that, for a given final time and total volume of injection, because of the shut-in periods, during the injection periods, the flow rate is higher than the conventional constant injection rate. Particularly at early times when the interface has smaller radius, this higher flow rate (and thus higher velocity) promotes the destabilization, leading to more severe overall fingering. However, the philosophy behind the cyclic injection is that, during the shut-in periods, the driving force for the growth of instabilities, i.e., the pumping, is removed, and thus, due to the stabilizing effect of interfacial tension, the instabilities developed during the injection period are supposed to shrink. Although such shrinkage might have occurred, its amount is not significant compared with the increased growth of the fingers due to the higher injection rate in the previous injection stage. To elaborate on this point, let us try to find curvature-driven relaxation time which is the required shut-in time to fully retract the fingers developed during the injection stage. Assume that a full cycle takes t_c which can be split into the time interval of $[0, t_I]$ during which the fluid is injected with the constant flow rate of Q and the time interval of $[t_I, t_c]$ during which the injection is stopped. At the end of the shut-in stage, the perturbation amplitude can be written as

$$\zeta_{n_{\max}}(t_c) = \zeta_{n_{\max}}(0)\exp\left(\int_0^{t_c} \lambda_{n_{\max}} dt'\right). \tag{51}$$

The integral term can be split into

$$\int_0^{t_c} \lambda_{n_{\max}} dt' = \int_0^{t_I} \lambda_{n_{\max}} dt' + \int_{t_I}^{t_c} \lambda_{n_{\max},I} dt' = I_1 + I_2. \tag{52}$$

The first integral on the right-hand side shows the finger growth during the injection stage, while the second integral shows the retraction of the fingers due to the relaxation effect of interfacial tension during the shut-in stage. Accordingly, in the first integral, $\lambda_{n_{\max}}$ is a function of time, but in the second integral, it is a constant which only depends on $n_{\max}$ at t_I. To retract all the fingers and fully smooth the pattern, the value of $\zeta_{n_{\max}}(t_c)$ must get to zero. Therefore, equating Eq. (52) with zero and simplifying the integrals gives the curvature-driven relaxation time, i.e., $t_\sigma = t_c - t_I$ as follows (the derivation details are presented in Appendix B):

$$t_\sigma = \frac{\frac{4A}{3\sqrt{3}}[\mathcal{H}(R_I) - \mathcal{H}(R_0)] - \ln\frac{R_I}{R_0} - \frac{2A}{3\sqrt{3}\Psi}\left[\frac{\mathcal{H}(R_I)}{R_I} - \frac{\mathcal{H}(R_0)}{R_0}\right] + \frac{A}{\sqrt{3}}\ln\frac{[\mathcal{H}(R_I)-1][\mathcal{H}(R_0)+1]}{[\mathcal{H}(R_I)+1][\mathcal{H}(R_0)-1]}}{\frac{A(R_I^2 - R_0^2)}{6\sqrt{3}\Psi R_I^3}\mathcal{H}(R_I)(\Psi R_I - 2)}t_I, \tag{53}$$
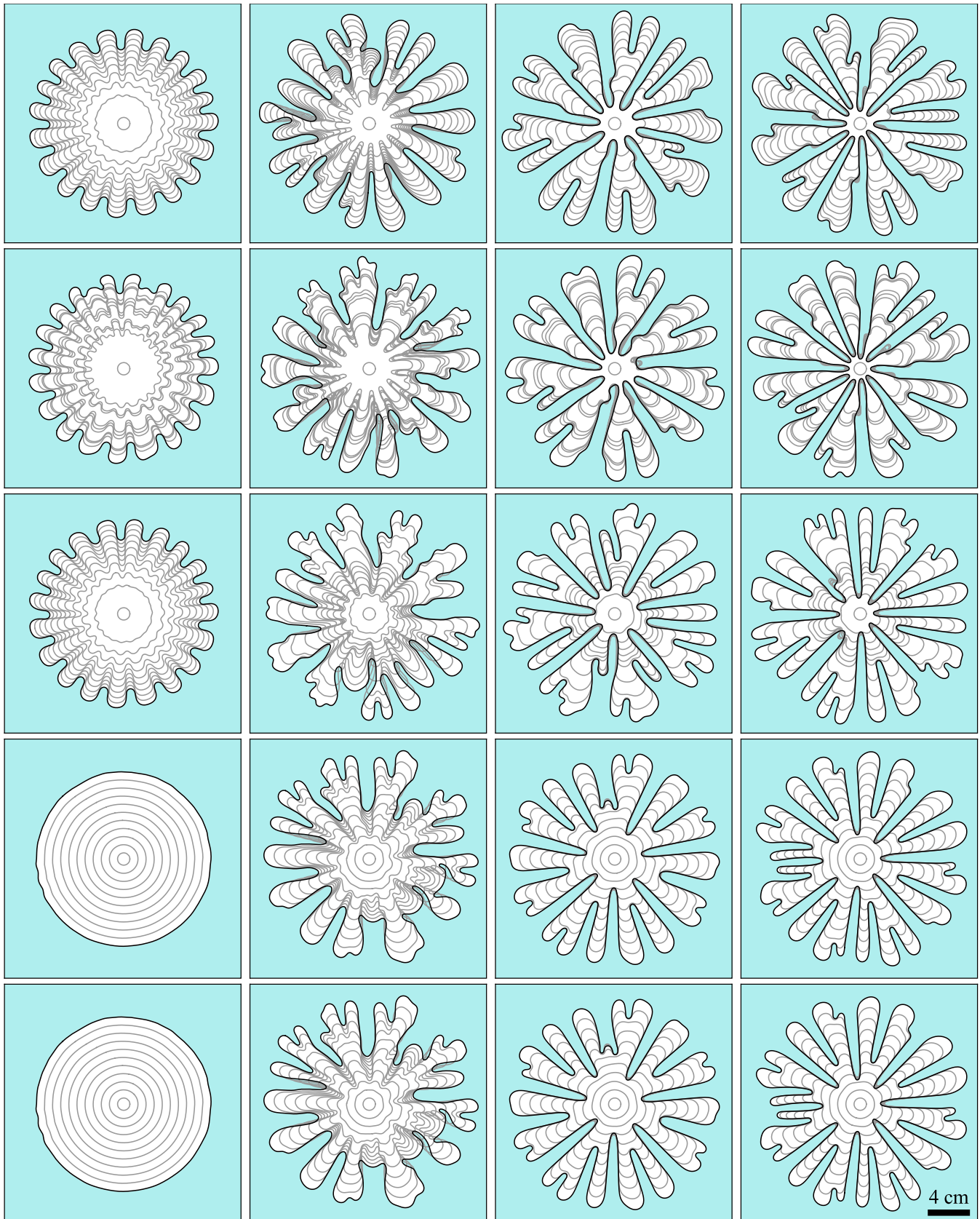
FIG. 4. Temporal evolution of interfacial patterns for different mobility ratios under the action of different injection flow rate schemes. The rows, from top to bottom, represent constant, cyclic, two-rate, linear, and nonlinear (this study), respectively. The columns, from left to right, correspond to MR = 2, MR = 10, MR = 100, and MR = 1000, respectively.
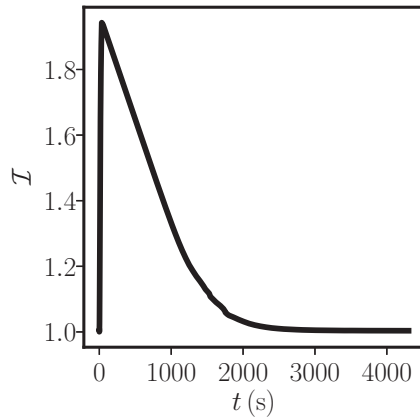
FIG. 5. Variation of $\mathcal{I}$ for a process in which a long shut-in period follows the constant injection period (MR = 2).

where

$$\Psi = \frac{A\left(R_{\mathrm{I}}^2 - R_0^2\right)}{2\gamma t_{\mathrm{I}}}, \tag{54}$$

$$\mathcal{H}(R) = \sqrt{1 + \Psi R}. \tag{55}$$

For the conditions of this paper, the employed shut-in period of 4.91 s is at least four times smaller than t_σ obtained from the above equation, leading to a negligible effect of interfacial tension stabilizing action during the shut-in stages. It is worth noting that t_σ obtained from the above equation is the minimum time required to fully retract the fingers. In practice, because of the reduction of the number of the fingers over time, the actual curvature-driven relaxation time is several orders of magnitude higher than t_σ obtained from the above equation. To provide an estimate for the order of magnitude of the actual t_σ, for the case shown in the top left corner of Fig. 4 (i.e., the constant injection rate for MR = 2), at the end of the flow process, the pump was shut down, and the simulation was continued until the interface became a perfect circle. According to the corresponding variation of $\mathcal{I}$ which was illustrated in Fig. 5, it takes $\sim$4000 s for the stabilizing effect of the interfacial tension to fully retract the fingers (i.e., once $\mathcal{I} = 1$) which developed for an injection time of only 34.4 s (for more details, see the video clips presented in the Supplemental Material [53]). For higher mobility ratios with more severe fingering, the actual t_σ can be even much longer. This observation implies that, to have an effective cyclic injection policy, the shut-in periods must be much longer than the injection periods. Additionally, the magnitude of the minimum required shut-in period depends on the severity of the fingering in the previous injection period.

As mentioned before, four cycles as the typical number of cycles were considered in the cyclic injection scenario. However, the number of cycles in the range of 2–7 was tested for MR = 1000 as the typical mobility ratio. The corresponding patterns which were illustrated in Fig. 6 do not show any remarkable difference, indicating that the number of cycles has a negligible effect on the performance of the cyclic injection scenario.

By examining the last three rows of Fig. 4, it is quite evident that all two-rate, linear, and nonlinear policies reduced the fingering phenomenon to some extent. The two-rate policy did not reduce the initial number of developed fingers, but the fully swept central area is larger than that of the constant injection rate except for MR = 2 in which the flow rates of the first and second stages were the same and equal to the constant injection rate, leading to the same performance of two-rate and constant injection schemes.

Linear and nonlinear policies not only reduced the initial number of fingers for all values of MR, but also the developed fingers are shorter, and the fully swept central area is higher than the corresponding area in the constant injection rate protocol. The physical explanation for this observation is that, according to Fig. 3, for these protocols at the beginning of the process, the instantaneous flow rate is less than the constant injection rate, leading to more stable interface at early times. However, to inject the same volume for a given time, at later times for all these protocols, the instantaneous flow rate becomes higher than the constant injection rate, but because it happens at higher radii, it is not able to destabilize the interface considerably. The overall effect is that the interface is more stable than the constant injection rate policy.

Another important observation is that the performance of linear and nonlinear protocols is different for different values of MR. For MR = 2, linear and nonlinear schemes fully stabilized the interface, and the interface is almost perfectly circular, while for higher values of MR, although both schemes reduced the fingering by making shorter fingers and delayed tip-splitting, they were not able to fully stabilize the interface. The reason seems to be related to the differences between the operational time of the injection protocols and the curvature-driven relaxation time of the interfaces. For MR = 2, for a long time after the beginning of the process, the deviation of the interface from the ideal circle is still low, and thus, the curvature-driven relaxation time is short and comparable
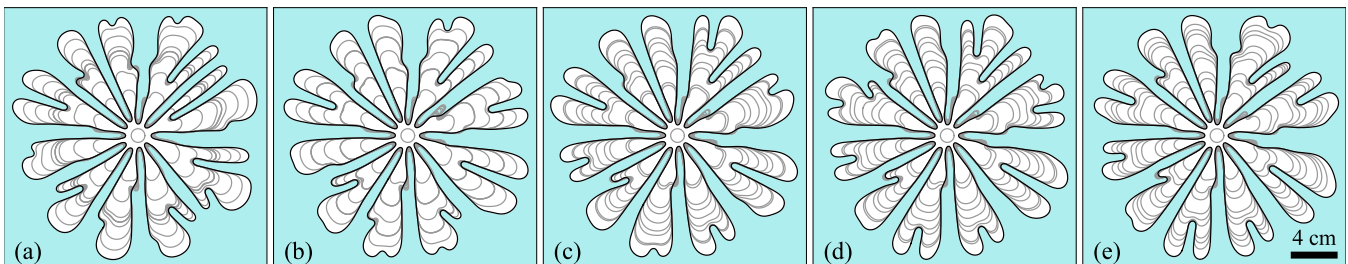

FIG. 6. Effect of number of cycles on the performance of the cyclic injection scenario for the number of cycles of (a) 2, (b) 3, (c) 5, (d) 6, and (e) 7.

with the operational time of the protocols. Consequently, both linear and nonlinear protocols fully stabilized the interface. For higher values of MR, a very short time after the beginning of the process, the nonlinear effects dominate the dynamics, and thus, because of the higher deviation from the circular shape, the curvature-driven relaxation time becomes much longer than the operational time of the protocols, leading to a reduction in their effectiveness.

For quantitative investigation of the performance of the employed stabilization policies, the temporal variation of the invading fluid saturation profile was calculated and plotted in Fig. 7. For MR = 2, while cyclic and two-rate protocols do not show any remarkable difference, the linear and nonlinear schemes show a flat saturation profile which is an indicator of pistonlike displacement. For MR = 10, for the cyclic injection, the saturation profile has a stairlike shape, indicating a more fingered interface, while for linear and nonlinear schemes, the saturation profile has become gentler, indicating a more stable interface.

For MR = 100 and 1000, a steep single-step change in saturation profile of the constant and cyclic policies is observed at around $R = 0.015$ which is an indicator of severe fingering. For the two-rate policy, although the same single-step change is observed, it is slightly gentler. Linear and nonlinear schemes show two distinct improvements. First, the onset radius of fingering was increased to around $R = 0.025$. Second, instead of a single-step steep variation in saturation, a two-step change is observed, and thus, for a given radius, it took a longer time to experience lower saturations. This behavior indicates that employing these policies has changed the single-step finger generation of constant injection into two-step generation of fingers which reduces the unpleasant effect of fingering remarkably. It is worth noting that the radial length of the second step change in saturation is less for MR = 1000 than that for MR = 100 mainly because of severe nonlinear effects for higher values of MR.

Another important observation is that, for constant and cyclic policies, as time advances, after the steep change in saturation profile, a valley is created which is an indication of finger base thinning over time and disappearance of small fingers due to the competition with larger fingers. This phenomenon is much weaker for the other protocols, and for a given radius, only a small reduction in saturation is seen over time because of the stabilizing effect which resulted in a smaller number of fingers with thicker bases resistant to thinning.

The controlling ability of the employed protocols can be investigated more quantitively in Figs. 8 and 9 which illustrate the variation of $\mathcal{I}$, $\mathcal{C}$, and E_A as functions of time and MR, repectively. The quantitative comparison of these measures again agrees with the above qualitative observations. It is apparent that, for all protocols except the cyclic protocol, the value of $\mathcal{I}$ is less than that of constant injection rate. Additionally, it is apparent that linear and nonlinear policies give the least $\mathcal{I}$, particularly for lower values of MR, meaning that these polices give the least interfacial area. A similar trend is observed for $\mathcal{C}$, and for all protocols except the cyclic scheme, the value of $\mathcal{C}$ is less than that of constant injection rate. In terms of E_A, cyclic injection has a smaller E_A than constant injection rate, while all other protocols resulted in

higher values of E_A, particularly for MR = 2. Additionally, it is apparent that linear and nonlinear policies give the highest E_A, particularly for lower values of MR, meaning that these polices give the highest sweep efficiency. Only for MR = 10 at the end of the process the performance is comparable with the other schemes which is related to the occurrence of the capillary fingering which was not considered in derivation of the flow rate schemes.

Another observation is that, for all cases, the last two schemes outperformed the two-rate scheme. The reason seems to be related to the fact that the two-rate policy is merely a poor approximation of the linear policy, and thus, although it performs better than the conventional constant injection rate policy, it cannot perform the same as the more exact linear-approximate, linear-exact, and nonlinear policies.

To illustrate the evolution of individual modes and extract the dominant mode, we performed Fourier mode analysis. The Fourier coefficient C_n, which shows the relative strength of mode n, was calculated according to [28]

$$C_n(t) = \frac{1}{2\pi} \int_{-\pi}^{\pi} \mathcal{R}(\phi, \, t) \exp{(in\phi)} d\phi. \qquad (56)$$

Figure 10 shows the evolution of individual modes. While the dominant mode is easily distinguishable for symmetric patterns, most of the patterns are nonsymmetric, leading to the coexistence of many modes with similar strength. However, all the mode evolution graphs are consistent with their corresponding patterns. For each pattern, at the end of the process, the dominant mode corresponds to the number of fingers in the pattern. This can be confirmed by Fig. 11, which shows the relative amplitudes of individual modes at the end of the simulation.

We now turn our attention to the second set of our simulations which attempts to investigate the performance of different flow rate protocols for a range of different capillary numbers (Ca). Figure 12 shows the employed flow rate policies in this set of simulations (set Ca). As mentioned previously, MR = 100 was employed for all cases in this set. Like set MR, for all tested values of Ca, the ideal flow rate policy obtained by Dias *et al.* [25], Batista *et al.* [26], and this paper coincide. Like set MR, for the range of $[R_0 = 0.004, R_f = 0.02833]$, the calculated value of $A\dot{R}R^2/\gamma$ is in the range of $[32, 2 \times 10^5]$, implying the validity of the approximation of Dias *et al.* [25] for the conditions of set Ca, leading to the same approximate policy of Dias *et al.* [25] and the exact policy of Batista *et al.* [26]. Additionally, like set MR, it seems that the contribution of nonlinear terms in Eq. (18) is negligible compared with the linear term, leading to a nonsignificant difference in the obtained policy compared with linear policies. Only for the Ca = 1.5×10^{-3} a very small difference was observed between the nonlinear policy introduced in this paper and the linear policies. It is worth mentioning that only for unrealistic viscosity values a little difference was observed in the obtained protocols for the linear-approximate, linear-exact, and nonlinear cases, concluding that the linear-approximate protocol proposed by Dias *et al.* [25] is accurate enough for practical applications. Another important observation in Fig. 12 is that the piecewise constant policy shows very little dependence on the values of
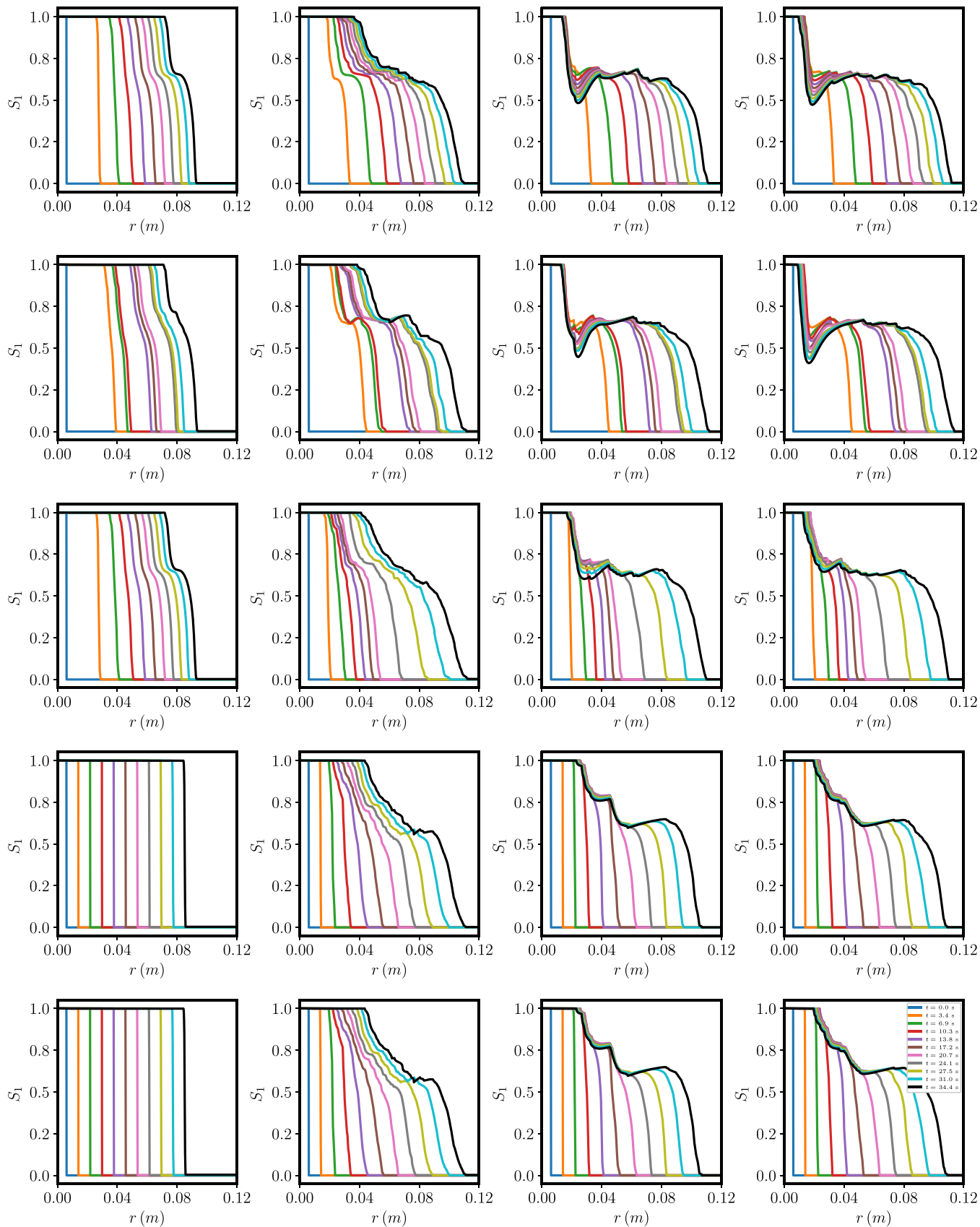
FIG. 7. Temporal variation of the invading fluid saturation profile for different mobility ratios under the action of different injection flow rate schemes. The rows, from top to bottom, represent constant, cyclic, two-rate, linear, and nonlinear (this study), respectively. The columns, from left to right, correspond to MR = 2, MR = 10, MR = 100, and MR = 1000, respectively.

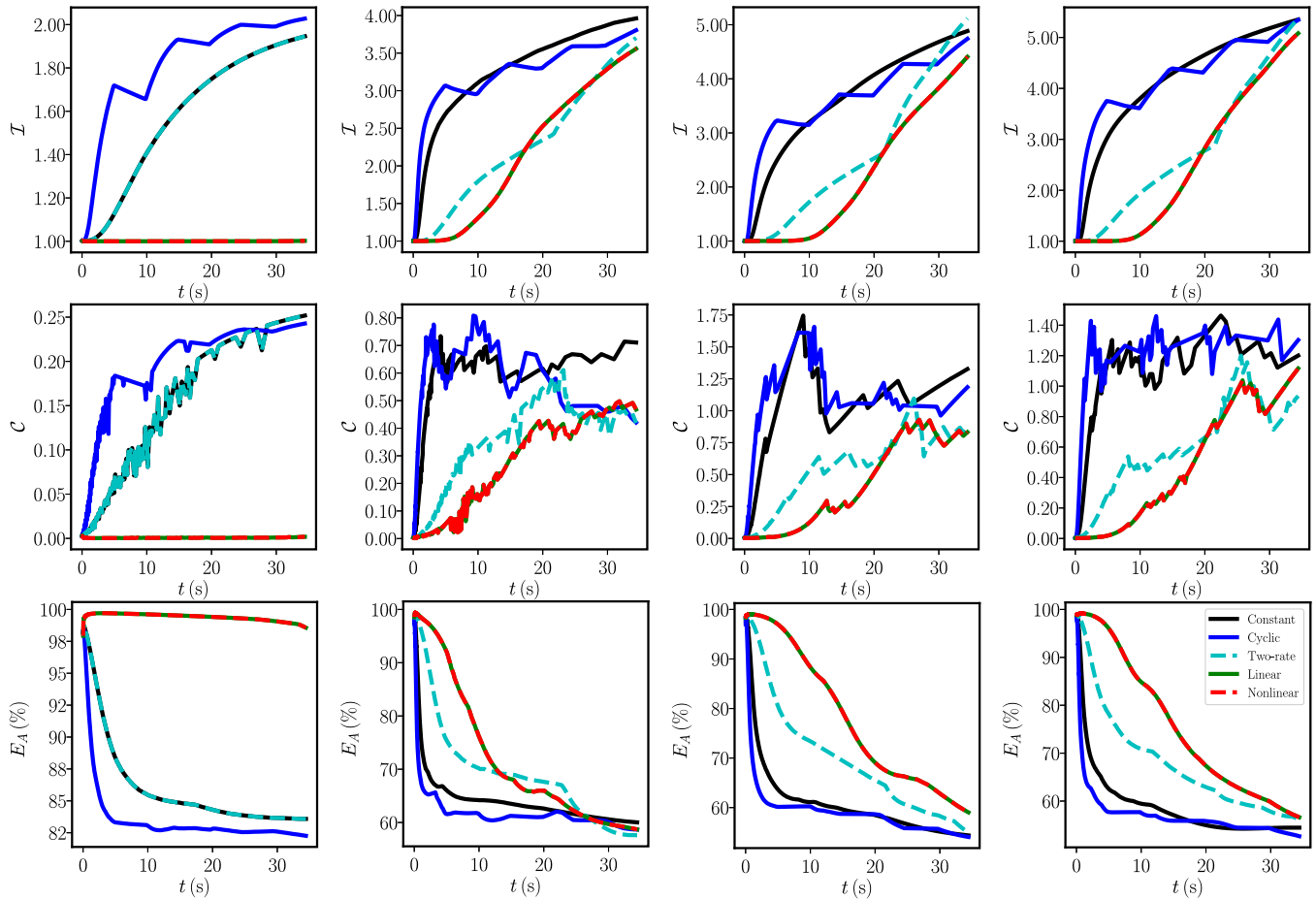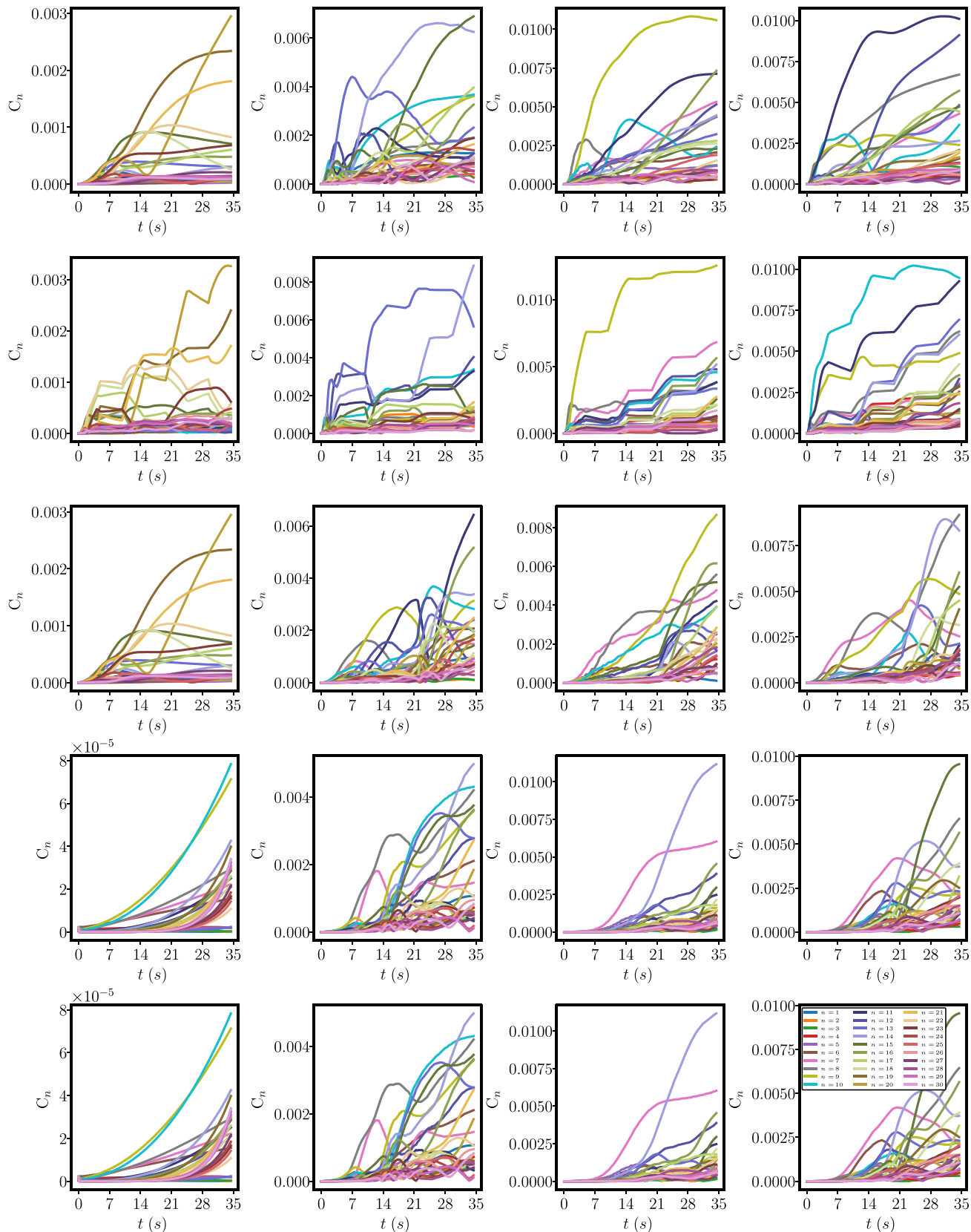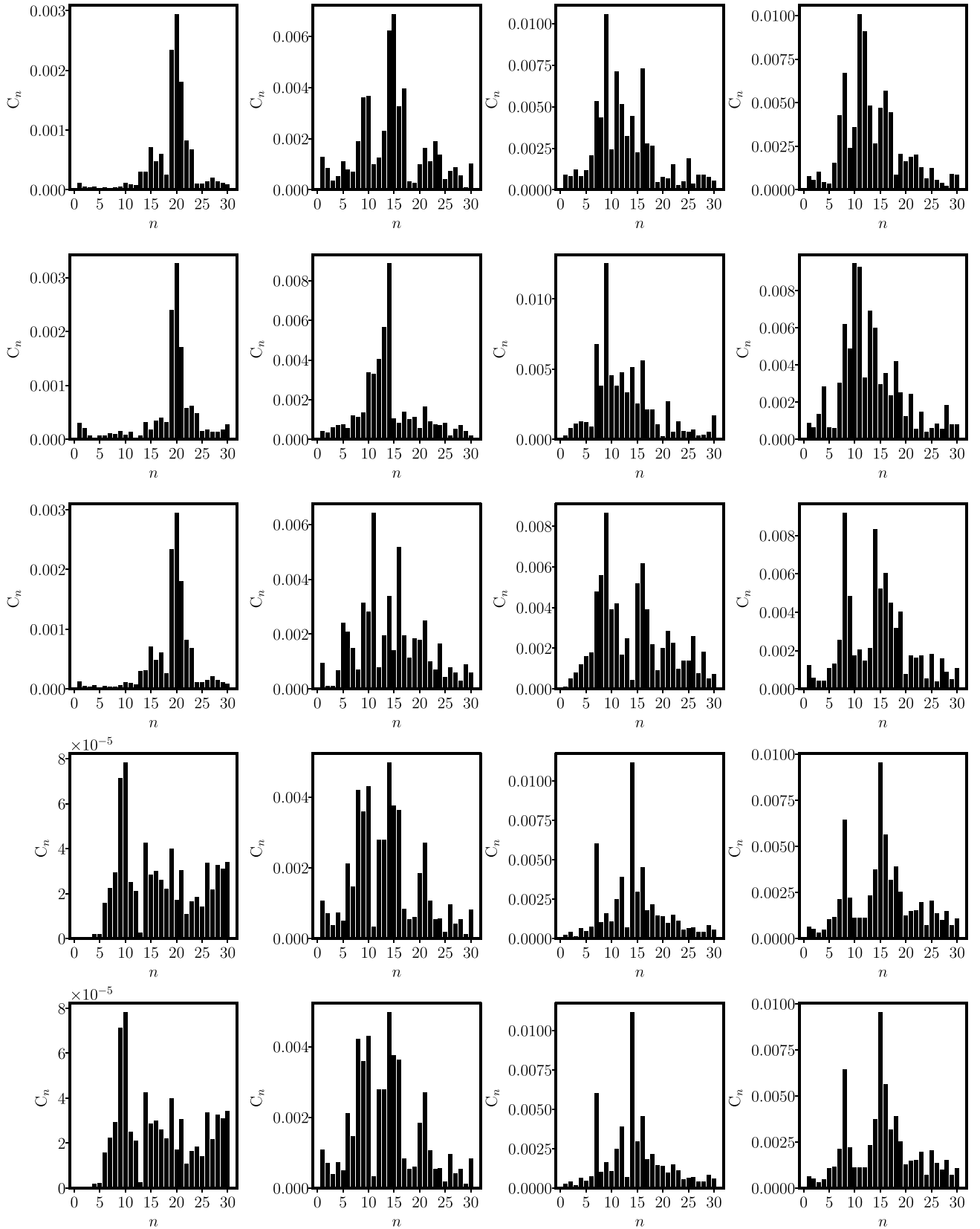FIG. 8. Temporal variation of $\mathcal{I}$, $\mathcal{C}$ and E_A for different mobility ratios under the action of different injection flow rate schemes. The columns, from left to right, correspond to MR = 2, MR = 10, MR = 100, and MR = 1000, respectively.

Ca. Similarly, in Fig. 3, we observed that the policy did not change with MR variation except for Fig. 3(a). This is because the piecewise constant policy is essentially an approximation of the linear policy, which does not exhibit any dependence on fluid properties. Therefore, the piecewise constant policy behaves similarly.

Temporal evolution of the interfacial patterns for different capillary numbers under the action of different flow rate protocols is illustrated in Fig. 13. Like set MR, the linear scheme refers to both linear-approximate and linear-exact schemes. By examining the top row of Fig. 13, we observe that, for the conventional constant injection rate, except for Ca $= 1.5 \times 10^{-3}$, all patterns evolve to fingered structures, although like the previous set, the physical characteristics of the patterns are different for different values of Ca. While Ca $= 1.5 \times 10^{-2}$ shows only the finger-spreading
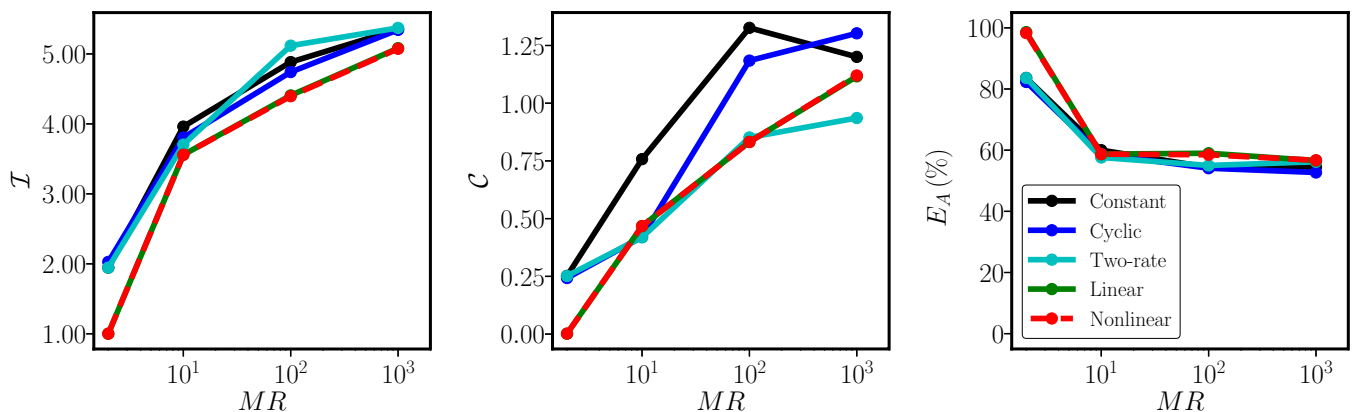
FIG. 9. Quantitative measures of $\mathcal{I}$, $\mathcal{C}$, and E_A at final time as a function of MR.

FIG. 10. Time evolution of the mode amplitudes for different mobility ratios under the action of different injection flow rate schemes. The rows, from top to bottom, represent constant, cyclic, two-rate, linear, and nonlinear (this study), respectively. The columns, from left to right, correspond to MR = 2, MR = 10, MR = 100, and MR = 1000, respectively.
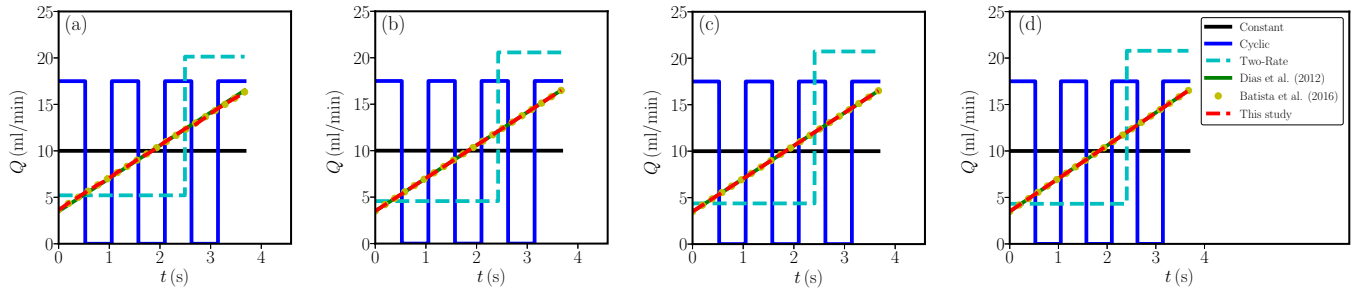
FIG. 11. Final amplitudes of each mode for different mobility ratios under the action of different injection flow rate schemes. The rows, from top to bottom, represent constant, cyclic, two-rate, linear, and nonlinear (this study), respectively. The columns, from left to right, correspond to MR = 2, MR = 10, MR = 100, and MR = 1000, respectively.

FIG. 12. Employed injection flow rate policies for different values of Ca, (a) Ca = 0.0015, (b) Ca = 0.015, (c) Ca = 0.15, and (d) Ca = 1.5.

mechanism, Ca $= 1.5 \times 10^{-1}$ and 1.5 show secondary instability mechanisms of shielding, tip splitting, and side branching in addition to spreading. Except Ca $= 1.5 \times 10^{-3}$, all the other patterns tend to saturate, reaching almost a stagnation point. An important observation is that, with increasing Ca, the width of fingers reduces which agrees well with both theoretical and experimental predictions of smaller finger width for higher capillary numbers [1,40].

In terms of the performance of different policies, like set MR, the cyclic protocol intensified the instability, expedited the tip-splitting mechanism, and reduced the fully swept central area for all tested values of Ca which can be related to the same physical and theoretical explanation discussed for the previous set. Examination of the last three rows of Fig. 13 shows that all two-rate, linear, and nonlinear policies reduced the fingering phenomenon and ended up with shorter fingers for the two cases of Ca $= 1.5 \times 10^{-2}$ and 1.5×10^{-1} but did not show any remarkable effect on the pattern for Ca = 1.5. Contrary to what we observed for set MR, for set Ca, none of the tested policies changed the initial number of the developed fingers, but for Ca $= 1.5 \times 10^{-2}$, two-rate, linear, and nonlinear schemes delayed the finger tip splitting.

Another important observation is that the performance of two-rate, linear, and nonlinear protocols is different for different values of Ca. For Ca $= 1.5 \times 10^{-3}$, all these schemes fully stabilized the interface, and the interface is almost perfectly circular. For Ca $= 1.5 \times 10^{-2}$, although all these schemes reduced the fingering by making shorter fingers and delayed tip splitting, they were not able to fully stabilize the interface. For Ca $= 1.5 \times 10^{-1}$ and particularly for Ca = 1.5 for all schemes, the performance is almost the same as the constant injection rate scheme. Like set MR, the reason seems to be related to the differences between the operational time of the protocols and the curvature-driven relaxation time.

Figure 14 shows the time variation of the invading fluid saturation profile for the patterns in Fig. 13. For Ca $= 1.5 \times 10^{-3}$, for all policies including the constant injection rate, the saturation profile remains flat during the process, indicating that the displacement is pistonlike. For Ca $= 1.5 \times 10^{-2}$, for the constant injection and the cyclic schemes, a step change in saturation is observed which is sharper for the later one. Although the same step change is observed for the two-rate, linear, and nonlinear policies, it is gentler. For Ca $= 1.5 \times 10^{-1}$, almost all saturation profiles are similar with a little improvement for the two-rate, linear,

and nonlinear policies. For Ca = 1.5, the difference between the different policies is even lower, and the profiles are almost the same. Particularly the valleys in the saturation profile of the constant injection rate do not disappear in the other controlling schemes, implying that none of the employed schemes was able to stabilize the interface.

As a more quantitative measure of performance, we have calculated and plotted the variation of $\mathcal{I}$, $\mathcal{C}$, and E_A as functions of time and Ca in Figs. 15 and 16, respectively. For Ca $= 1.5 \times 10^{-3}$, although all policies resulted in the same value of $\mathcal{I}$, two-rate, linear, and nonlinear policies resulted in lower $\mathcal{C}$ and slightly higher E_A compared with the constant injection rate protocol. The cyclic scheme resulted in slightly higher $\mathcal{C}$ and lower E_A. For Ca $= 1.5 \times 10^{-2}$, compared with the constant injection protocol, two-rate, linear, and nonlinear policies resulted in lower $\mathcal{I}$, $\mathcal{C}$, and higher E_A, while the cyclic protocol resulted in higher $\mathcal{I}$, higher $\mathcal{C}$, and slightly lower E_A. For Ca $= 1.5 \times 10^{-1}$, compared with the constant injection rate, the cyclic injection resulted in lower $\mathcal{I}$, higher $\mathcal{C}$, and slightly higher E_A. The two-rate scheme, while performing better than the constant injection rate protocol over the time, resulted in almost the same values of $\mathcal{I}$, $\mathcal{C}$, and E_A at the end of the process. Both linear and nonlinear policies outperformed the constant injection rate scheme and resulted in lower $\mathcal{I}$, lower $\mathcal{C}$, and higher E_A. For Ca = 1.5, although over the course of time, all two-rate, linear, and nonlinear schemes showed lower $\mathcal{I}$, lower $\mathcal{C}$, and higher E_A compared with the constant injection rate, finally, they ended up with slightly higher $\mathcal{I}$, slightly lower $\mathcal{C}$, and almost the same E_A. The cyclic scheme almost performed the same as the constant injection rate scheme.

Like the previous case, Fourier mode analysis was performed to identify the evolution of individual modes. Figure 17 shows the time evolution of individual modes. Like the previous case, while symmetric patterns exhibit a single dominant mode, nonsymmetric patterns show several modes with comparable strength. Additionally, Fig. 18 shows the relative amplitudes of individual modes at t_f, confirming that the dominant mode corresponds to the number of fingers on the pattern.

Considering different patterns developed for set MR and set Ca together, a very important observation is that, for patterns whose constant injection counterpart exhibits linear flow regime, the two-rate, linear, and nonlinear controlling schemes work very well and suppress the fingering phenomenon remarkably. As the system transitions into a non-
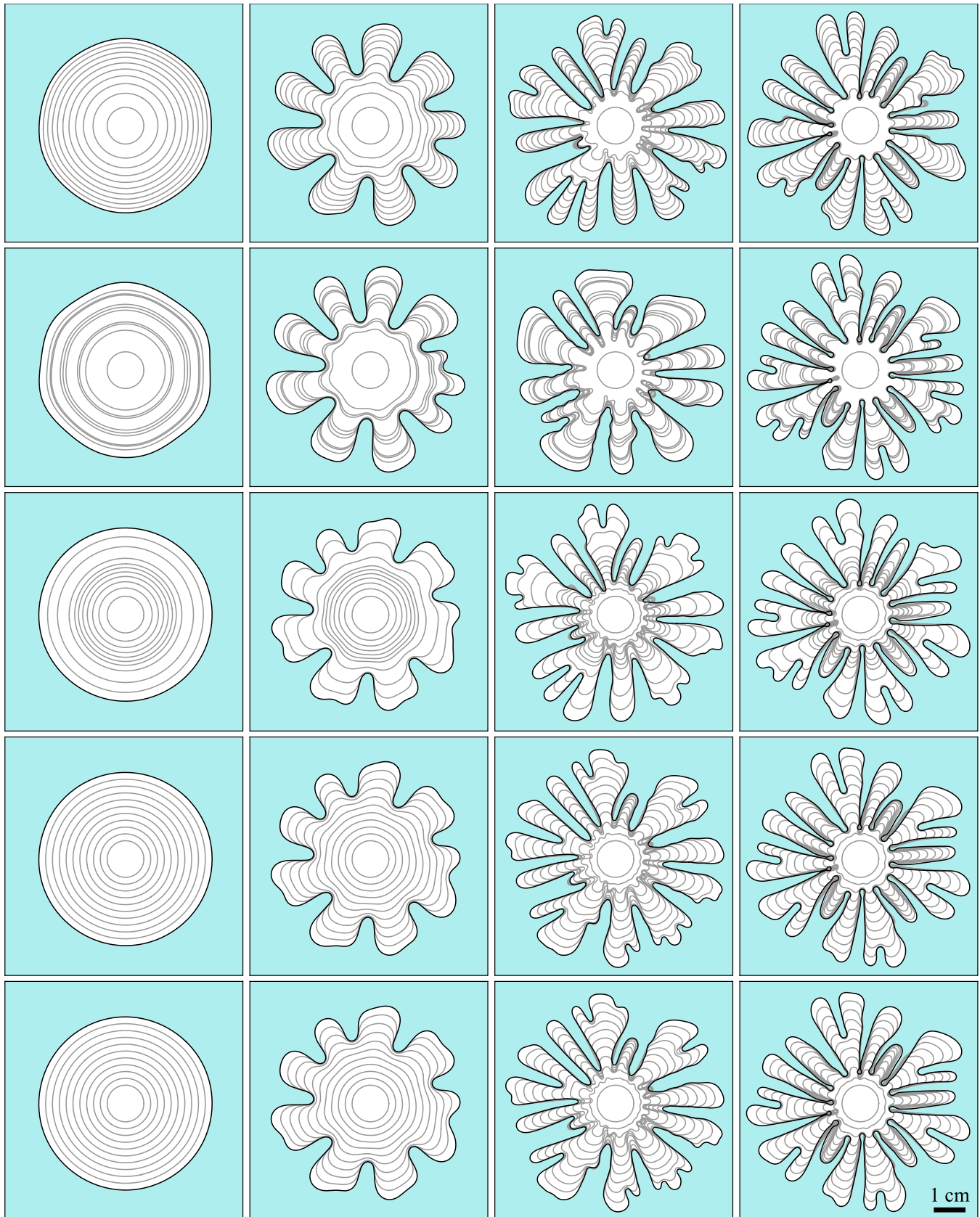
FIG. 13. Temporal evolution of interfacial patterns for different capillary numbers under the action of different injection flow rate schemes. The rows, from top to bottom, represent constant, cyclic, two-rate, linear, and nonlinear (this study), respectively. The columns, from left to right, correspond to Ca = 1.5 × 10^{-3}, Ca = 1.5 × 10^{-2}, Ca = 1.5 × 10^{-1}, and Ca = 1.5, respectively.
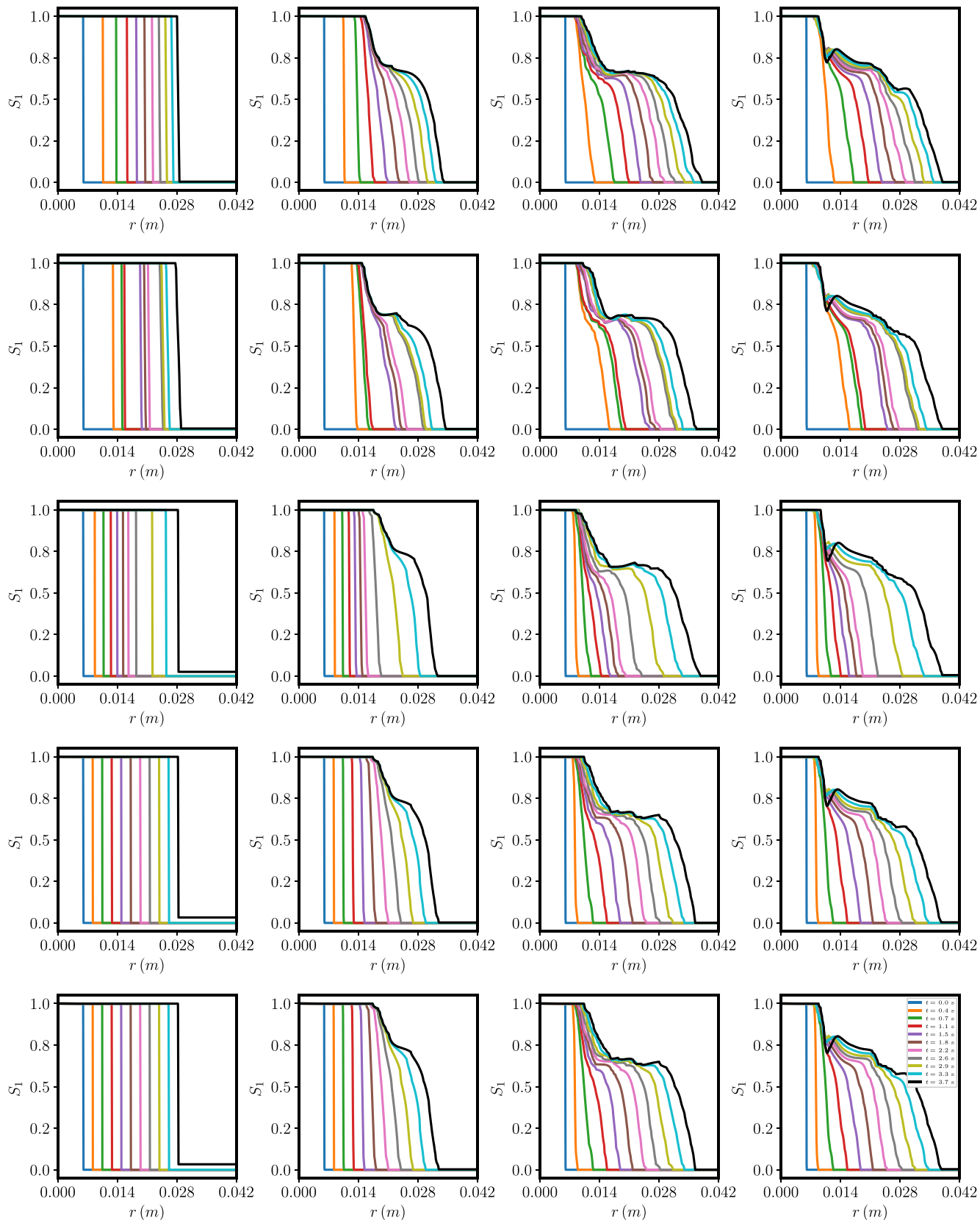
FIG. 14. Temporal variation of the invading fluid saturation profile for different capillary numbers under the action of different injection flow rate schemes. The rows, from top to bottom, represent constant, cyclic, two-rate, linear, and nonlinear (this study), respectively. The columns, from left to right, correspond to $Ca = 1.5 \times 10^{-3}$, $Ca = 1.5 \times 10^{-2}$, $Ca = 1.5 \times 10^{-1}$, and $Ca = 1.5$, respectively.
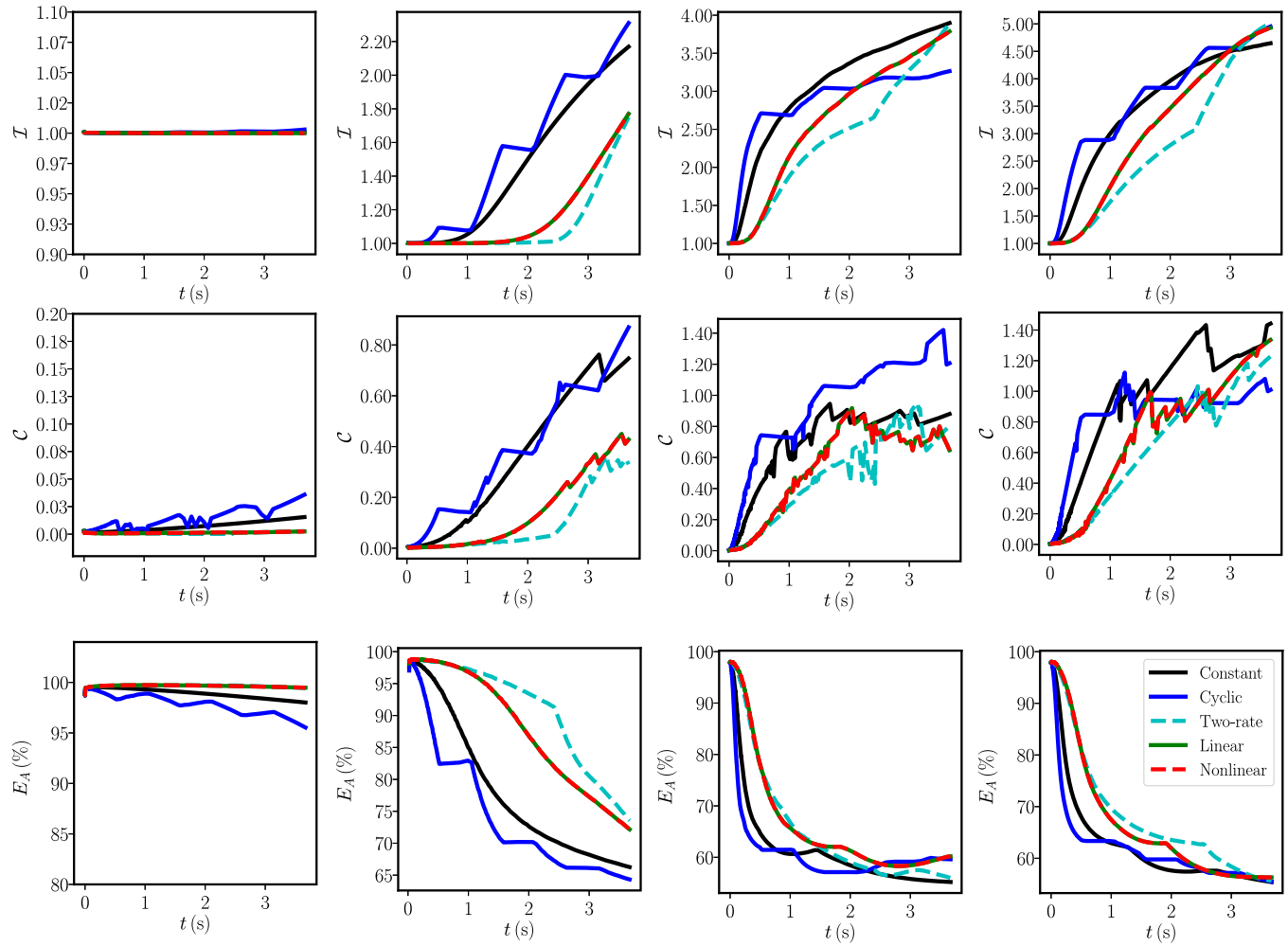
FIG. 15. Temporal variation of $\mathcal{I}$, $\mathcal{C}$ and E_A for different capillary numbers under the action of different injection flow rate schemes. The columns, from left to right, correspond to Ca = 1.5 × 10^{-3}, Ca = 1.5 × 10^{-2}, Ca = 1.5 × 10^{-1}, and Ca = 1.5, respectively.

linear regime, the schemes may continue to perform well, but their effectiveness is more pronounced in patterns where the constant injection counterpart exhibits lower nonlinearity than those with higher nonlinearity. As the nonlinearity increases, the curvature-driven relaxation time surpasses the operational time of the schemes, resulting in their reduced effectiveness.

This is consistent with the results of Dias *et al.* [25] and Morrow *et al.* [29]. Figures 4 in Refs. [25,29] suggest that the performance of the linear policy is higher for patterns whose constant injection counterpart exhibits less nonlinearity than those whose constant injection counterpart exhibits higher nonlinearity.
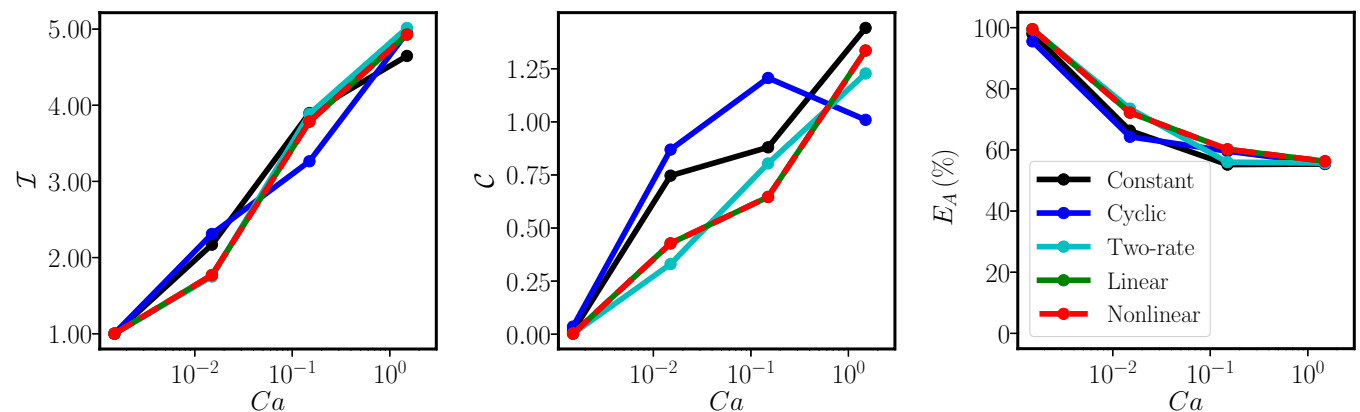

FIG. 16. Quantitative measures of $\mathcal{I}$, $\mathcal{C}$, and E_A at final time as a function of Ca.
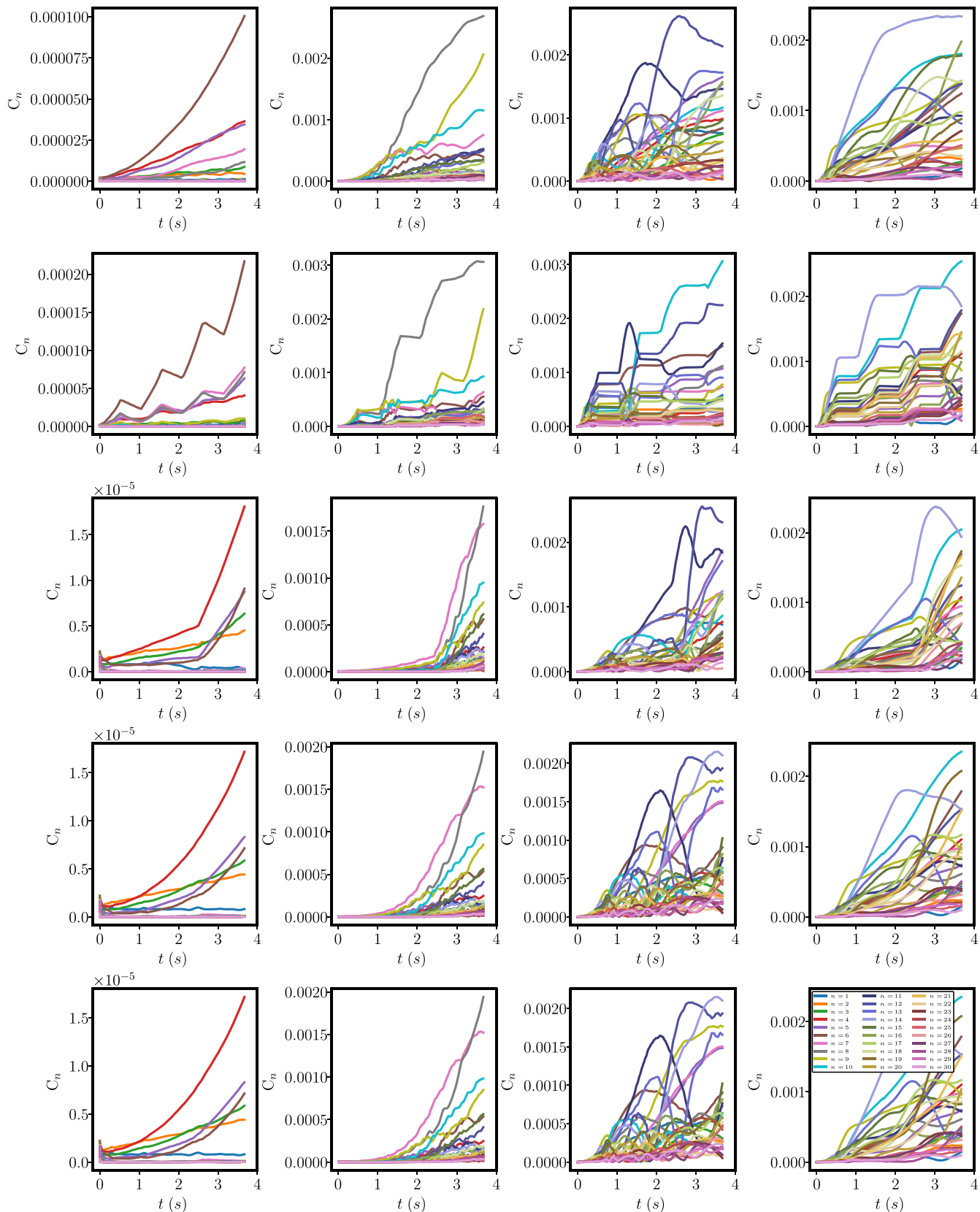
FIG. 17. Time evolution of the mode amplitudes for different capillary numbers under the action of different injection flow rate schemes. The rows, from top to bottom, represent constant, cyclic, two-rate, linear, and nonlinear (this study), respectively. The columns, from left to right, correspond to Ca = 1.5 × 10^{-3}, Ca = 1.5 × 10^{-2}, Ca = 1.5 × 10^{-1}, and Ca = 1.5, respectively.
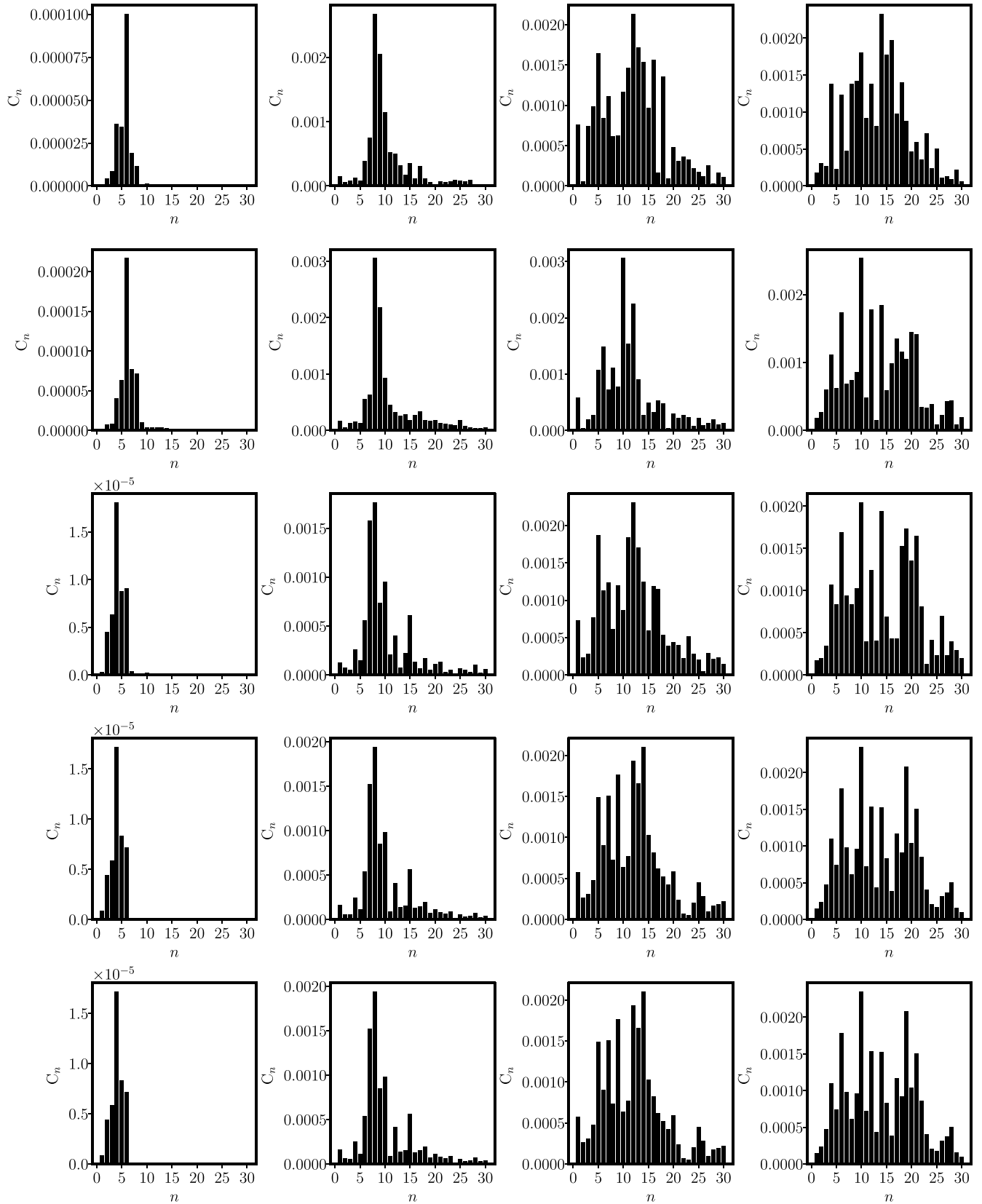
FIG. 18. Final amplitudes of each mode for different capillary numbers under the action of different injection flow rate schemes. The rows, from top to bottom, represent constant, cyclic, two-rate, linear, and nonlinear (this study), respectively. The columns, from left to right, correspond to $Ca = 1.5 \times 10^{-3}$, $Ca = 1.5 \times 10^{-2}$, $Ca = 1.5 \times 10^{-1}$, and $Ca = 1.5$, respectively.

IV. CONCLUSIONS

In this paper, we carried out a series of systematic numerical simulations to investigate the performance of various time-dependent injection flow rate strategies at an advanced time regime of the viscous fingering dynamics at which the instability has become fully nonlinear and the interface is extremely deformed. Motivated by the fact that the ultimate shape of the interface only depends on the capillary and viscous forces, we have combined all the governing parameters into two scaling groups, mobility ratio and capillary number, and systematically varied each of these parameters at a time while keeping the others fixed.

Our numerical findings showed that, compared with the conventional constant injection rate scheme, the cyclic injection strategy intensified the development of the interfacial instabilities for most of the cases which was attributed to the necessity of very long curvature-driven relaxation time required to fully retract the developed fingers. While two-rate, linear, and nonlinear schemes reduced the fingering phenomenon for linear flow regimes, their performance at nonlinear stages is strongly dependent on the degree of nonlinearity, and once severe nonlinearity develops, their performance reduces regardless of the value of the mobility ratio and/or the capillary number. This stems from the fact that, for each fingering pattern, the efficiency of these policies strongly depends on the differences between the time scales of the operational time of these policies and the required curvature-driven relaxation time of the fingering pattern. Patterns with less severe fingering have short curvature-driven relaxation time comparable with the operational time of the controlling schemes, leading to better stability response to the schemes, but patterns with more severe fingering have long curvature-driven relaxation time, and thus, the operational time of the schemes is not enough to fully stabilize the interface.

It is worth noting that, in linear scheme, pressure increases as the injection flow rate increases. On the other hand, in real field applications, there is a maximum operational pressure above which further pressure increase is not allowed. At some point, the linear scheme will reach this maximum pressure. The injection process would then have to be switched to the corresponding maximum allowed injection flow rate. For future work, an interesting topic would be to find the optimum time at which the injection can be switched from the linear scheme to the constant injection scheme to ensure the displacement stability.

APPENDIX A: CONVERGENCE TEST

Figure 19 illustrates the convergence behavior of the developed patterns as the edge length decreases. It can be observed that, for the largest tested edge length, the number of vertices is insufficient to capture the pattern details. As the edge length decreases, the number of vertices increases, and therefore, higher detail of the dynamics is captured. However, for the last two tested edge lengths, we do not see any remarkable difference, and the developed patterns are identical. It is worth noting that, because of the division by the edge length in the Cauchy-Green coordinates given in Ref. [39], the edge length cannot be reduced infinitely, and below a critical edge length, due to the division by very small values, the algorithm may become divergent again. Similarly, Fig. 20 shows the temporal convergence behavior. It is worth noting that, since in this paper we have employed an adaptive time step, instead of directly altering the time step, we assessed the convergence by varying the parameter α, which controls the time step. From Fig. 20, it is evident that the scheme is convergent. These convergence tests are consistent with the results of the convergence tests in Refs. [54,55].

APPENDIX B: DERIVATION OF t_σ

Assume that a full cycle takes t_c which can be split into the time interval of $[0, t_I]$, during which the fluid is injected with the constant flow rate of Q, and the time interval of $[t_I, t_c]$, during which the injection is stopped. At the end of the shut-in stage, the perturbation amplitude can be written as

$$\zeta_{n_{\max}}(t_c) = \zeta_{n_{\max}}(0)\exp\left(\int_0^{t_c} \lambda_{n_{\max}} dt'\right). \quad \text{(B1)}$$

The integral term can be split into

$$\int_0^{t_c} \lambda_{n_{\max}} dt' = \int_0^{t_I} \lambda_{n_{\max}} dt' + \int_{t_I}^{t_c} \lambda_{n_{\max,I}} dt' = I_1 + I_2. \quad \text{(B2)}$$

The first integral on the right-hand side shows the finger growth during the injection stage in which $\lambda_{n_{\max}}$ is a function
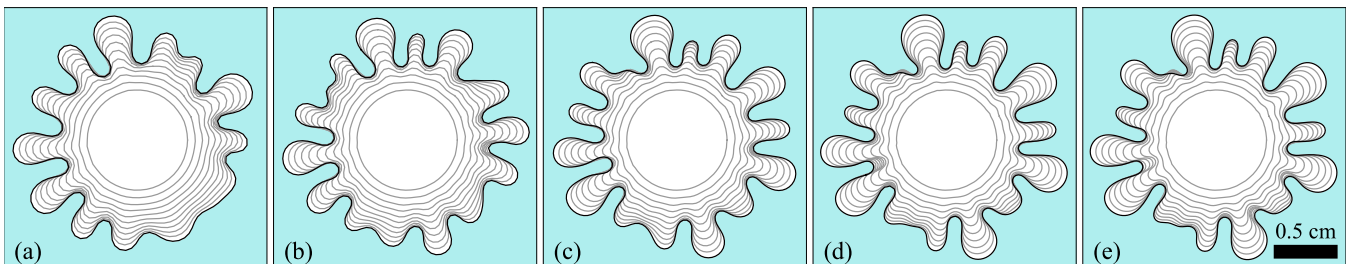

FIG. 19. Convergence test of the numerical scheme in terms of spatial resolution for the average edge length of (a) 500 μm, (b) 400 μm, (c) 300 μm, (d) 200 μm, and (e) 100 μm.
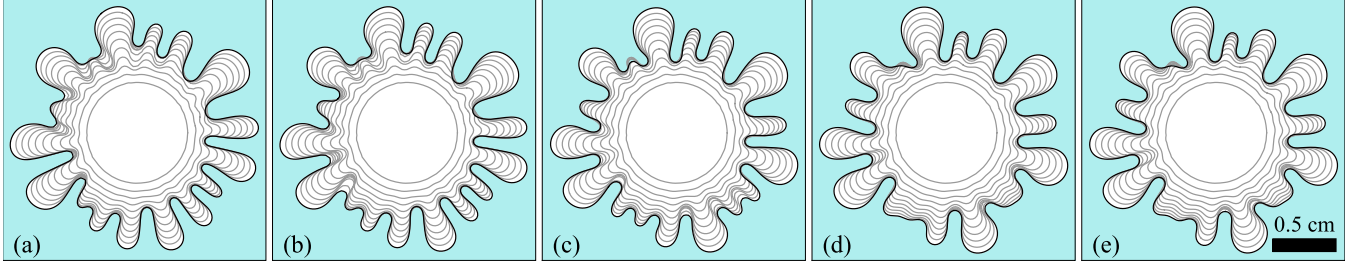
FIG. 20. Convergence test of the numerical scheme in terms of temporal resolution for different values of α: (a) 0.2, (b) 0.15, (c) 0.1, (d) 0.05, and (e) 0.025.

of time. Substituting Eq. (19) into Eq. (11) yields the following expression for $\lambda_{n_{\max}}$:

$$
\lambda_{n_{\max}} = \frac{Q}{2\pi R^2}\left[A\sqrt{\frac{1}{3}\left(1 + \frac{A\dot{R}R^2}{\gamma}\right)} - 1\right]
$$
$$
- \frac{\gamma}{R^3}\sqrt{\frac{1}{3}\left(1 + \frac{A\dot{R}R^2}{\gamma}\right)}\left[\frac{1}{3}\left(1 + \frac{A\dot{R}R^2}{\gamma}\right) - 1\right]. \tag{B3}
$$

Thus, the first integral I_1 can be written as

$$
I_1 = \int_0^{t_1}\left\{\frac{Q}{2\pi R^2}\left[A\sqrt{\frac{1}{3}\left(1 + \frac{A\dot{R}R^2}{\gamma}\right)} - 1\right]\right.
$$
$$
\left. - \frac{\gamma}{R^3}\sqrt{\frac{1}{3}\left(1 + \frac{A\dot{R}R^2}{\gamma}\right)}\left[\frac{1}{3}\left(1 + \frac{A\dot{R}R^2}{\gamma}\right) - 1\right]\right\}dt'. \tag{B4}
$$

From Eq. (20), we have

$$
dt = \frac{2\pi R}{Q}dR. \tag{B5}
$$

Substituting Eq. (B5) into Eq. (B4) and simplifying the obtained expression yields

$$
I_1 = \frac{4A}{3\sqrt{3}}[\mathcal{H}(R_I) - \mathcal{H}(R_0)]
$$
$$
- \ln\frac{R_I}{R_0} - \frac{2A}{3\sqrt{3}\Psi}\left[\frac{\mathcal{H}(R_I)}{R_I} - \frac{\mathcal{H}(R_0)}{R_0}\right]
$$

$$
+ \frac{A}{\sqrt{3}}\ln\frac{[\mathcal{H}(R_I) - 1][\mathcal{H}(R_0) + 1]}{[\mathcal{H}(R_I) + 1][\mathcal{H}(R_0) - 1]}, \tag{B6}
$$

where

$$
\Psi = \frac{A(R_I^2 - R_0^2)}{2\gamma t_I}, \tag{B7}
$$

$$
\mathcal{H}(R) = \sqrt{1 + \Psi R}, \tag{B8}
$$

where Ψ has a dimension of m^{-1}. The second integral I_2 shows the retraction of the fingers due to the stabilizing effect of interfacial tension during the shut-in stage in which $\lambda_{n_{\max,I}}$ is a constant which only depends on $n_{\max}$ at t_I; thus,

$$
I_2 = \int_{t_I}^{t_f}\lambda_{n_{\max,I}}dt' = \lambda_{n_{\max,I}}(t_f - t_I)
$$
$$
= -\frac{\gamma}{R_I^3}n_{\max,I}(n_{\max,I}^2 - 1)(t_f - t_I). \tag{B9}
$$

Substituting Eq. (19) into Eq. (B9) and simplifying the resulting expression yields

$$
I_2 = -\frac{A(R_I^2 - R_0^2)}{6\sqrt{3}\Psi R_I^3 t_I}\sqrt{1 + \Psi R_I}(\Psi R_I - 2)(t_f - t_I). \tag{B10}
$$

Substituting Eqs. (B6) and (B10) into Eq. (B2) and equating it with zero gives the curvature-driven relaxation time, i.e., $t_\sigma = t_c - t_I$ as follows:

$$
t_\sigma = \frac{\frac{4A}{3\sqrt{3}}[\mathcal{H}(R_I) - \mathcal{H}(R_0)] - \ln\frac{R_I}{R_0} - \frac{2A}{3\sqrt{3}\Psi}\left[\frac{\mathcal{H}(R_I)}{R_I} - \frac{\mathcal{H}(R_0)}{R_0}\right] + \frac{A}{\sqrt{3}}\ln\frac{[\mathcal{H}(R_I) - 1][\mathcal{H}(R_0) + 1]}{[\mathcal{H}(R_I) + 1][\mathcal{H}(R_0) - 1]}}{\frac{A(R_I^2 - R_0^2)}{6\sqrt{3}\Psi R_I^3}\mathcal{H}(R_I)(\Psi R_I - 2)}t_I. \tag{B11}
$$

[1] P. G. Saffman and G. I. Taylor, The penetration of a fluid into a porous medium or Hele-Shaw cell containing a more viscous liquid, Proc. R. Soc. Lond. A **245**, 312 (1958).

[2] B. Jha, L. Cueto-Felgueroso, and R. Juanes, Fluid Mixing from Viscous Fingering, Phys. Rev. Lett. **106**, 194502 (2011).

[3] E. J. Peters and D. L. Flock, The onset of instability during two-phase immiscible displacement in porous media, Soc. Pet. Eng. J. **21**, 249 (1981).

[4] F. Guerrero, J. Bryan, and A. Kantzas, Visualization of chemical heavy oil EOR displacement mechanisms in a 2D system, Energies (Basel) **14**, 950 (2021).

[5] S. Berg and H. Ott, Stability of CO_2-brine immiscible displacement, Int. J. Greenhouse Gas Control **11**, 188 (2012).

[6] D. Pihler-Puzović, P. Illien, M. Heil, and A. Juel, Suppression of Complex Fingerlike Patterns at the Interface between Air and a Viscous Fluid by Elastic Membranes, Phys. Rev. Lett. **108**, 074502 (2012).

[7] D. Pihler-Puzović, R. Périllat, M. Russell, A. Juel, and M. Heil, Modelling the suppression of viscous fingering in elastic-walled Hele-Shaw cells, J. Fluid Mech. **731**, 162 (2013).

[8] D. Pihler-Puzović, A. Juel, and M. Heil, The interaction between viscous fingering and wrinkling in elastic-walled Hele-Shaw cells, Phys. Fluids **26**, 022102 (2014).

[9] Z. Zheng, H. Kim, and H. A. Stone, Controlling Viscous Fingering using Time-Dependent Strategies, Phys. Rev. Lett. **115**, 174501 (2015).

[10] T. T. Al-Housseiny, P. A. Tsai, and H. A. Stone, Control of interfacial instabilities using flow geometry, Nat. Phys. **8**, 747 (2012).

[11] T. T. Al-Housseiny and H. A. Stone, Controlling viscous fingering in tapered Hele-Shaw cells, Phys. Fluids **25**, 092102 (2013).

[12] E. Alvarez-Lacalle, J. Ortın, and J. Casademunt, Low viscosity contrast fingering in a rotating Hele-Shaw cell, Phys. Fluids **16**, 908 (2004).

[13] P. H. A. Anjos, V. M. M. Alvarez, E. O. Dias, and J. A. Miranda, Rotating Hele-Shaw cell with a time-dependent angular velocity, Phys. Rev. Fluids **2**, 124003 (2017).

[14] S. D. R. Wilson, The Taylor-Saffman problem for a non-Newtonian liquid, J. Fluid Mech. **220**, 413 (1990).

[15] J. E. Sader, D. Y. C. Chan, and B. D. Hughes, Non-Newtonian effects on immiscible viscous fingering in a radial Hele-Shaw cell, Phys. Rev. E **49**, 420 (1994).

[16] T. H. Beeson-Jones and A. W. Woods, On the selection of viscosity to suppress the Saffman-Taylor instability in a radially spreading annulus, J. Fluid Mech. **782**, 127 (2015).

[17] P. Fast, L. Kondic, M. J. Shelley, and P. Palffy-Muhoray, Pattern formation in non-Newtonian Hele-Shaw flow, Phys. Fluids **13**, 1191 (2001).

[18] L. Kondic, M. J. Shelley, and P. Palffy-Muhoray, Non-Newtonian Hele-Shaw Flow and the Saffman-Taylor Instability, Phys. Rev. Lett. **80**, 1433 (1998).

[19] L. Surguchev, A. Koundin, O. Melberg, T. A. Rolfsvåg, and W. P. Menard, Cyclic water injection: Improved oil recovery at zero cost, Pet. Geosci. **8**, 89 (2002).

[20] I. Brailovsky, A. Babchin, M. Frankel, and G. Sivashinsky, Fingering instability in water-oil displacement, Transp. Porous Media **63**, 363 (2006).

[21] J. Bataille, Stability of a radial immiscible drive, Rev. Inst. Fr. Pet. Ann. Combust. Liq. **23**, 1349 (1968).

[22] A. Leshchiner, M. Thrasher, M. B. Mineev-Weinstein, and H. L. Swinney, Harmonic moment dynamics in Laplacian growth, Phys. Rev. E **81**, 016206 (2010).

[23] S. Li, J. S. Lowengrub, J. Fontana, and P. Palffy-Muhoray, Control of Viscous Fingering Patterns in a Radial Hele-Shaw Cell, Phys. Rev. Lett. **102**, 174501 (2009).

[24] E. O. Dias, F. Parisio, and J. A. Miranda, Suppression of viscous fluid fingering: A piecewise-constant injection process, Phys. Rev. E **82**, 067301 (2010).

[25] E. O. Dias, E. Alvarez-Lacalle, M. S. Carvalho, and J. A. Miranda, Minimization of Viscous Fluid Fingering: A Variational Scheme for Optimal Flow Rates, Phys. Rev. Lett. **109**, 144502 (2012).

[26] C. Batista, E. O. Dias, and J. A. Miranda, Hamiltonian formulation towards minimization of viscous fluid fingering, Phys. Rev. E **94**, 013109 (2016).

[27] M. Mirzadeh and M. Z. Bazant, Electrokinetic Control of Viscous Fingering, Phys. Rev. Lett. **119**, 174501 (2017).

[28] T. Gao, M. Mirzadeh, P. Bai, K. M. Conforti, and M. Z. Bazant, Active control of viscous fingering using electric fields, Nat. Commun. **10**, 4002 (2019).

[29] L. C. Morrow, T. J. Moroney, and S. W. McCue, Numerical investigation of controlling interfacial instabilities in non-standard Hele-Shaw configurations, J. Fluid Mech. **877**, 1063 (2019).

[30] T. H. Beeson-Jones and A. W. Woods, Control of viscous instability by variation of injection rate in a fluid with time-dependent rheology, J. Fluid Mech. **829**, 214 (2017).

[31] Í. M. Coutinho and J. A. Miranda, Control of viscous fingering through variable injection rates and time-dependent viscosity fluids: Beyond the linear regime, Phys. Rev. E **102**, 063102 (2020).

[32] A. Pouplard and P. A. Tsai, Viscous fingering instability of complex fluids in a tapered geometry, arXiv:2205.08019.

[33] A. Pouplard and P. A. Tsai, Controlling viscous fingering instabilities of complex fluids, arXiv:2205.08005.

[34] E. M. A. Mokheimer, M. Hamdy, Z. Abubakar, M. R. Shakeel, M. A. Habib, and M. Mahmoud, A comprehensive review of thermal enhanced oil recovery: Techniques evaluation, J. Energy Res. Technol. **141**, 030801 (2018).

[35] S. Jain, H. Pachisia, A. Sharma, S. Patel, S. Patel, and B. Ragunathan, A systematic review—Chemical EOR using surfactants and polymers, Mater. Today Proc. **62**, 7220 (2022).

[36] A. Segall, O. Vantzos, and M. Ben-Chen, Hele-Shaw flow simulation with interactive control using complex barycentric coordinates, in *Symposium on Computer Animation* (The Eurographics Association, Zurich, Switzerland, 2016), pp. 85–95.

[37] J. Miranda and M. Widom, Radial fingering in a Hele-Shaw cell: A weakly nonlinear analysis, Physica D **120**, 315 (1998).

[38] E. O. Dias and J. A. Miranda, Control of radial fingering patterns: A weakly nonlinear approach, Phys. Rev. E **81**, 016312 (2010).

[39] A. Segall and M. Ben-Chen, 2D Simulation and mapping using the Cauchy-Green complex barycentric coordinates, Ph.D. Dissertation, Computer Science Department, Technion, 2016.

[40] I. Bischofberger, R. Ramachandran, and S. R. Nagel, An island of stability in a sea of fingers: Emergent global features of the viscous-flow instability, Soft Matter **11**, 7428 (2015).

[41] Y.-S. Huang and C.-Y. Chen, A numerical study on radial Hele-Shaw flow: Influence of fluid miscibility and injection scheme, Comput. Mech. **55**, 407 (2015).

[42] R. Tsuzuki, Q. Li, Y. Nagatsu, and C.-Y. Chen, Numerical study of immiscible viscous fingering in chemically reactive Hele-Shaw flows: Production of surfactants, Phys. Rev. Fluids **4**, 104003 (2019).

[43] J.-D. Chen, Growth of radial viscous fingers in a Hele-Shaw cell, J. Fluid Mech. **201**, 223 (1989).

[44] H. Kim, T. Funada, D. D. Joseph, and G. M. Homsy, Viscous potential flow analysis of radial fingering in a Hele-Shaw cell, Phys. Fluids **21**, 074106 (2009).

[45] E. O. Dias and J. A. Miranda, Wavelength selection in Hele-Shaw flows: A maximum-amplitude criterion, Phys. Rev. E **88**, 013016 (2013).

[46] P. H. A. Anjos, E. O. Dias, and J. A. Miranda, Radial fingering under arbitrary viscosity and density ratios, Phys. Rev. Fluids **2**, 084004 (2017).

[47] M. J. P. Gingras and Z. Rácz, Noise and the linear stability analysis of viscous fingering, Phys. Rev. A **40**, 5960 (1989).

[48] R. Lenormand, E. Touboul, and C. Zarcone, Numerical models and experiments on immiscible displacements in porous media, J. Fluid Mech. **189**, 165 (1988).

[49] R. Lenormand, Liquids in porous media, J. Phys.: Condens. Matter **2**, SA79 (1990).

[50] V. Hernández-Mederos and J. Estrada-Sarlabous, Sampling points on regular parametric curves with control of their distribution, Comput. Aided Geom. Des. **20**, 363 (2003).

[51] S. J. Jackson, D. Stevens, H. Power, and D. Giddings, A boundary element method for the solution of finite mobility ratio immiscible displacement in a Hele-Shaw cell, Int. J. Numer. Methods Fluids **78**, 521 (2015).

[52] S. J. Jackson, H. Power, D. Giddings, and D. Stevens, The stability of immiscible viscous fingering in Hele-Shaw cells with spatially varying permeability, Comput. Methods Appl. Mech. Eng. **320**, 606 (2017).

[53] See Supplemental Material at http://link.aps.org/supplemental/10.1103/PhysRevE.107.065108 for two video files.

[54] M. Zhao, W. Ying, J. Lowengrub, and S. Li, An efficient adaptive rescaling scheme for computing moving interface problems, Commun. Comput. Phys. **21**, 679 (2017).

[55] S. Li, J. S. Lowengrub, and P. H. Leo, A rescaling scheme with application to the long-time simulation of viscous fingering in a Hele-Shaw cell, J. Comput. Phys. **225**, 554 (2007).